CrossMark

J. Fluid Mech. (2019), *vol.* 873, *pp.* 287–321. © Cambridge University Press 2019
doi:10.1017/jfm.2019.408

Interaction of coherent flow structures in adverse pressure gradient turbulent boundary layers

Matthew Bross[1],†, Thomas Fuchs[1] and Christian J. Kähler[1]

[1]Institute of Fluid Mechanics and Aerodynamics, Universität der Bundeswehr München, 85577 Neubiberg, Germany

(Received 10 November 2018; revised 11 May 2019; accepted 11 May 2019; first published online 24 June 2019)

With the aim to characterize the near-wall flow structures and their interaction with large-scale motions in the log-law region, time-resolved planar and volumetric flow field measurements were performed in the near-wall and log-law region of an adverse pressure gradient turbulent boundary layer following a zero pressure gradient turbulent boundary layer at a friction Reynolds number $Re_\tau = 5000$. Due to the high spatial and temporal resolution of the measurements, it was possible to resolve and identify uniform-momentum zones in the region $z/\delta < 0.15$ or $z^+ < 350$ and to relate them with well known coherent flow motions near the wall. The space–time results confirm that the turbulent superstructures have a strong impact even on the very near-wall flow motion and also their alternating appearance in time and intensity could be quantified over long time sequences. Using the time record of the velocity field, rare localized separation events appearing in the viscous sublayer were also analysed. By means of volumetric particle tracking velocimetry their three-dimensional topology and dynamics could be resolved. Based on the results, a conceptual model was deduced that explains their rare occurrence, topology and dynamics by means of a complex interaction process between low-momentum turbulent superstructures, near-wall low-speed streaks and tilted longitudinal and spanwise vortices located in the near-wall region.

Key words: boundary layer structure, flow–structure interactions, turbulent boundary layers

1. Introduction

Turbulent flows along a flat plate with zero pressure gradient (ZPG) have been investigated in great detail in the last seven decades since the pioneering experiments by Klebanoff (1955). Today, many statistical and structural properties of the flow are well known, as documented in the extensive review by Wallace (2012). Of particular focus in the last two decades have been large-scale coherent motions called superstructures (Adrian, Meinhart & Tomkins 2000; Ganapathisubramani *et al.* 2005; Hutchins & Marusic 2007*a*; Monty *et al.* 2009; Buchmann *et al.* 2016). These superstructures appear as high- and low-momentum flow motions within the log-law

† Email address for correspondence: matthew.bross@unibw.de

https://doi.org/10.1017/jfm.2019.408 Published online by Cambridge University Press

region. A remarkable feature of these structures is that they can extend up to several boundary layer thicknesses in the streamwise direction. In addition, they strongly meander in the spanwise direction and it has been shown that they can carry a relatively large a portion of the layer's turbulent kinetic energy, especially at large Reynolds numbers. In effect, they contribute mainly to the second peak in the streamwise velocity fluctuations forming at high Reynolds numbers (Fernholz & Finley 1996). Therefore, the investigation of these superstructures is important for understanding the overall dynamics of turbulent boundary layers. Of particular interest is how these structures interact with the near-wall flow motion in the viscous sublayer and buffer layer.

The coupling of the outer and inner layer of a turbulent boundary layer was already noted in early hot-wire measurements by Rao, Narasimha & Narayanan (1971) where they observed intermediate 'bursts' of activity, which at low Reynolds number were consistent with the intermediate activity at the edge of the inner layer observed by Kline *et al.* (1967). However, over a larger Reynolds range $Re_\theta = 600$–9000, Rao *et al.* (1971) observed that the mean 'burst' period scales with outer units instead of inner (or viscous) units and suggested that the energy production in a turbulent boundary layer can only be understood by a interaction between inner and outer layers.

While the existence of the inner peak of the streamwise turbulent fluctuations around $z^+ = 15$ can be understood by means of the near-wall streaky flow structures and their meandering nature, as observed by Kline *et al.* (1967), the cause of the secondary peak was not well understood for a long time. As the scale separation between the inner and outer layer grows with increasing Reynolds number, the second energetic peak in the turbulent kinetic energy spectrum becomes more prominent. The emergence of a second energetic peak for high Reynolds number turbulent boundary layers is a topic under debate in the community since Hutchins *et al.* (2009) showed that, depending on the resolution of the measurement technique, a plateau rather than a peak appears. However, it is evident from many experimental investigations that energy residing in long streamwise wavelengths begins to appear in the log-law layer as the Reynolds number increases in ZPG turbulent boundary layers (Monty *et al.* 2009; Samie *et al.* 2018). While the inner peak scales with inner units the outer peak/plateau scales with outer units or δ (Hutchins & Marusic 2007*a*; Samie *et al.* 2018). With the observation of turbulent superstructures in the log-law region and the fact that they are meandering (Hutchins *et al.* 2011) like the near-wall low-speed streaks, the existence of the second peak/plateau became understandable as well.

A fascinating property of the superstructures is their streamwise length, which is on average approximately 6δ–8δ. However, instantaneously they can be 10δ–20δ. Similar structures appear in turbulent pipe and channel flow and are often called very large-scale motions (VLSM). However, Monty *et al.* (2009) showed the VLSMs in pipe and channel flows have slightly longer streamwise energy wavelengths and reside slightly further away from the wall than superstructures in turbulent boundary layers. This is likely due to the absence of intermittency in pipe and channel flows which is present in turbulent boundary layers. In addition, several researchers have considered elongated structures that reside in the outer region that are only a few boundary layer thicknesses in length, which are called large-scale motions (LSM) (Kovasznay, Kibens & Blackwelder 1970; Balakumar & Adrian 2007). In this investigation, superstructures refer to the elongated structures in the log-law region that are associated with the presence of a streamwise energy spectral peak/plateau in the log-law region of turbulent boundary layers. Moreover,

https://doi.org/10.1017/jfm.2019.408 Published online by Cambridge University Press

superstructures in the log-law region have been observed to modulate amplitude of the near-wall motion (Hutchins & Marusic 2007*b*), which becomes more prominent with increasing Reynolds number up to $Re_\tau = 10^6$ (Mathis, Hutchins & Marusic 2009). It was also observed that the near-wall fluctuations are correlated with the motion of turbulent superstructures (Ganapathisubramani *et al.* 2012).

All the findings outlined so far could be obtained from hot-wire measurements by using Taylor's frozen pattern hypothesis. While hot-wire measurements provide highly resolved temporal information about the flow at selected locations, particle image or tracking velocimetry based field measurements (PIV/PTV) are able to measure the flow velocity at thousands of points simultaneously. This is very useful for structural analysis as powerful multi-point techniques can be applied to the measured flow field for the investigation of spatial correlations, spatial Fourier mode analysis or other feature detection methods. A very basic feature detection method is looking for regions with uniform momentum. Using this approach, the instantaneous flow field can be separated in regions of uniform-momentum zones separated by thin shear layers. These regions were studied by Meinhart & Adrian (1995) and Adrian *et al.* (2000) in great detail. By subtracting a proper local streamwise convection velocity, several regions of uniform momentum can appear that are usually layered on top of each other if the measurements are performed in a streamwise wall-normal plane. More recently, uniform-momentum zones (UMZs) were identified and characterized over a range of large Reynolds numbers ($Re_\tau = 10^3$–10^4) in de Silva, Hutchins & Marusic (2016) and later the detection of the interfaces between these zones was analysed in depth in de Silva *et al.* (2017). The average number of UMZs detected in these studies increased from 3 to 5 with increasing Reynolds number. The detection of UMZs was also used to model the large-scale motions (LSM) present in the outer layer in turbulent boundary layer (Saxton-Fox & McKeon 2017).

In all of the previous mentioned work UMZs have been identified from individual instantaneous PIV images. Recently, Laskari *et al.* (2018) studied the temporal coherence of UMZs using time-resolved PIV of a ZPG turbulent boundary layer. They found that by taking the temporal lifetime of velocity peaks into account the average number of zones detected decreases when only using snapshot PIV images because the short lived zones are removed when taking the temporal coherence into account. These results provide a framework for scaling of coherent structures based on spatial extent and temporal lifetime of these regions. It was shown that a large number of zones detected is associated with large-scale $Q2$ events (correlated flow regions of low-momentum moving away from the wall) and conversely low number of detected zones indicates large-scale $Q4$ events (correlated flow regions of high-momentum moving towards the wall). Furthermore, they mention that the organization of the boundary layer with a low or high number of UMZs can be interpreted as a low- or high-momentum large-scale structure moving through the measurement plane. However, due to spatial resolution limitations the region below $z/\delta < 0.20$ could not be well resolved in past experiments. Although this region is of particular interest, resolving the near-wall region is challenging experimentally because of the strong velocity gradients and bias errors that can appear (Kähler, Scharnowski & Cierpka 2012*a*). Furthermore, the measurement uncertainty increases near the wall (Kähler, Scharnowski & Cierpka 2012*b*). However, it follows from the known coherent structures in the near-wall region and their dynamics that UMZs must also exist close to the wall. Also the modulation of the near-wall coherent motion by superstructures must lead to specific UMZs in the buffer layer and down to the viscous sublayer. Therefore, it is of interest to study UMZs near the wall and their sensitivity to modulations by turbulent superstructures.

https://doi.org/10.1017/jfm.2019.408 Published online by Cambridge University Press

Another interesting question is if the interaction of the coherent flow motions, detectable in the layered UMZs, can explain the existence of reverse flow events. Reverse flow events are relatively rare instances of small localized turbulent flow events at the wall with a velocity component in upstream direction. In recent years, the numerical prediction of reverse flow events in turbulent channel (Lenaers *et al.* 2012), pipe (Jalalabadi & Sung 2018), toroidal pipes (Chin *et al.* 2018) and ZPG boundary layer flows (Spalart & Coleman 1997) has achieved strong attention. As the spatial extent of these events is very small according to Cardesa *et al.* (2014), and their occurrence extremely seldom (Lenaers *et al.* 2012), their detection in experiments was quite challenging. However, in recent years their existence could be confirmed experimentally by using long-range micro PIV (Willert 2015; Willert *et al.* 2018) and micro pillar (Brücker 2015) techniques. The probability of such events occurring (calculated by the probability density function (p.d.f.) of the streamwise velocity or wall shear stress) was measured in a ZPG turbulent boundary layer to be approximately 0.01 % (Willert 2015) and 0.012 %–0.018 % (Willert *et al.* 2018). In addition, it was calculated to be 0.06 % in a direct numerical simulation (DNS) channel flow (Lenaers *et al.* 2012). Due to the small number a statistical analysis of reverse flow events is not really possible and the question still remains as to whether these events are generated in a universal manner or not.

The aforementioned numerical and experimental studies were performed at relatively low Reynolds numbers ($Re_\tau < 2500$ or $Re_\theta < 8000$) and mostly ZPG conditions. However, it is important to investigate these features at large Reynolds numbers for several reasons: (i) aerodynamic applications usually occur at high Reynolds numbers, (ii) the magnitude of the turbulent fluctuations increases with increasing Reynolds number (Vallikivi, Hultmark & Smits 2015; Samie *et al.* 2018) and (iii) to demonstrate that reverse flow events are not just a low Reynolds number effect. Furthermore, the current experimental investigations only yield information about the footprint of the reverse flow events on the wall shear stress (Brücker 2015) and the characteristics of the structures in an arbitrary slice selected by the light sheet used for the planar PIV investigations by Willert (2015) and Willert *et al.* (2018). To better understand the complex features of the near-wall region it is important to consider the three-dimensionality of the flow. This is supported by the DNS computations in Diaz-Daniel, Laizet & Vassilicos (2017), where a strong correlation between reverse flow events and strong spanwise flow motions was found in a ZPG turbulent boundary layer at Re_τ up to 680. They further provided evidence that these events may be related to quasi-streamwise oriented vortices in the near-wall region.

To enhance the detection probability of reverse flow events it is possible to consider larger Reynolds numbers. However, increasing the Reynolds number by accelerating the flow complicates their detection in experiments as the thickness of the near-wall region shrinks. To avoid this problem it is possible to enlarge their number by using a slight adverse pressure gradient (APG) flow. This is supported by the recent numerical investigation by Vinuesa, Örlü & Schlatter (2017*b*) where they showed that the reverse flow event probability over a wing with increasing APG conditions (Clauser pressure parameter $\beta = \delta^*/\tau_o \partial p/\partial x = 0.6$–$35$) can reach up to 30 %. They also observed that reverse flow events with a strong spanwise component were most probable at low APG but this strong spanwise component progressively decreases as the flow approaches separation near the trailing edge of the wing, which is thought to be a manifestation of flow separation mechanisms. However, the details of the transition from the fully attached to the partly and fully separated flow states is widely unknown (Skåre & Krogstad 1994; Michael & Rainer 2002), making the study

https://doi.org/10.1017/jfm.2019.408 Published online by Cambridge University Press

of APG boundary layers of interest. Furthermore, as rare reverse flow events resemble the incipient detachment events which proceed large-scale flow detachment described in Simpson (1989) they might serve as the nucleus for the generation of macroscopic flow separation in APG turbulent boundary layers, which makes the investigation of reverse flow events in APG turbulent boundary layers of general interest also for aerodynamic research. Finally, the effect of a pressure gradient on statistical quantities and coherent flow motions is by far less examined and understood compared to ZPG turbulent boundary layers. As turbulent boundary layer flows with pressure gradients determine the aerodynamic performance of many technical components, the physical understanding of these types of flows is of great scientific and technological interest and importance.

Experimental measurements of APG turbulent boundary layers in Monty, Harun & Marusic (2011), Harun *et al.* (2013), Knopp *et al.* (2015) study the influence of the pressure gradient on large-scale structures and momentum transport as well as parametric variation for the development of scaling models. However, strong agreement between various experimental and numerical databases about a scaling framework is absent. Recently, Maciel *et al.* (2018) established a framework for the outer scaling of APG turbulent boundary layers based on various experimental and numerical databases, but due to the lack of high quality near-wall data at large Reynolds numbers, they mention that the derived framework for scaling and governing parameters is not complete. This illustrates the need to perform high resolution near-wall flow measurements with accurate measurement techniques.

Recent technological progress in image acquisition and quantitative flow visualization allows for the possibility of fully three-dimensional time-resolved velocity measurements (Fuchs, Hain & Kähler 2016*a*; Kähler *et al.* 2016; Novara *et al.* 2016; Schanz, Gesemann & Schröder 2016). Moreover, the quality of the PTV measurement techniques has reached a high level, as shown in this investigation, such that flow effects in the viscous sublayer and buffer layer of a turbulent boundary layer can be examined experimentally, even at larger Reynolds numbers. Furthermore, the motivation for measuring in the near-wall region is to resolve the three-dimensional structures of near-wall flow events and how they relate to superstructures in the log-law layer. It seems likely that the reverse flow events are associated with the interaction of near-wall low-speed streaks (Kline *et al.* 1967; Smith & Metzler 1983) and low-momentum large-scale structures characterized by Buchmann *et al.* (2016) using large-scale PIV. In Bross & Kähler (2016) a conceptual model was proposed that assumes that the reverse flow events appear when low-speed streaks, low-momentum superstructures and near-wall vortices interact in a specific manner. In the investigation presented herein, the topology and statistics of near-wall reverse events will be discussed in more detail and their connection with both the flow in the wall-normal and spanwise directions will be outlined based on extensive measurements.

Since the high resolution volumetric measurement was limited to the near-wall region an additional planar measurement that extends from the near-wall region to the log-law region was performed to resolve the flow motion of the superstructures and their effect on the near-wall flow in time. In this near-wall investigation, up to three possible UMZs are detectable which can be explained by the layering of high- and low-speed streaks with high- and low-momentum superstructures. Depending on the layering of these structures, a region of low-momentum fluid persists from the near wall to the log-law layer, making the appearance of these rare reverse flow events possible. As these reverse flow events appear very seldom in low Reynolds

https://doi.org/10.1017/jfm.2019.408 Published online by Cambridge University Press

number turbulent boundary layers along flat plates with zero pressure gradient we examine these structures under the effect of an adverse pressure gradient to make a statistical analysis of the rare reverse flow events possible. This allows us to examine if these events are universal or if multiple generation mechanisms exist. In addition, it will also be possible to examine their scale and dynamics and if the events appear randomly in space and time or in packets with a characteristic frequency. A packet-like appearance is expected if a correlation exists between low-momentum superstructures and reverse flow events. To resolve the spatial and temporal details of the near-wall flow with high accuracy and spatial resolution, a novel tomographic tracking technique was developed that is able to determine the three-dimensional (3-D) flow motion also within the viscous sublayer (Fuchs, Hain & Kähler 2016*b*, 2017). Furthermore, information about the flow in the spanwise direction is accessible from the results presented herein, which is absent from previous two-dimensional (2-D) PIV studies.

2. Experimental systems and methods

Turbulent boundary layer experiments were performed at the Bundeswehr University Munich in the Atmospheric Wind tunnel Munich (AWM). The Eiffel type wind tunnel has a 22 m long test section with a cross-section of approximately 2 m $\times$ 2 m. Flow velocities up to 40 m s^{-1} can be achieved. A 7 m long polished aluminium boundary layer model consisting of two S-shaped deflections on either end of a 4 m flat plate zero pressure gradient (ZPG) section, was installed along the side wall of the wind tunnel. The adverse pressure gradient (APG) region (downstream of the ZPG part starting at $X = 5.75$ m and ending at $X = 7$ m, with an initial boundary layer thickness of 180 mm for $Re_\tau = 5000$) was fitted with a glass viewing window of size 0.26 m $\times$ 0.59 m, see figure 1. The X-direction indicates the streamwise distance along the wind tunnel, starting at the beginning of the model. The incoming ZPG flow history and global boundary layer parameters at the measurement locations in the APG, such as the edge velocity $U_f = 0.99U$, δ_{99}, δ^*, θ, $\partial p/\partial x^+$ and β, were measured in Reuther *et al.* (2015) for the same boundary layer model and Reynolds number and are reported in table 1.

In order to perform high resolution flow measurements, a local seeding system was installed upstream of the boundary layer wall, providing uniform seeding with a high tracer particle concentration near the wall, see Reuther & Kähler (2018). This local seeding system is located approximately 2 m upstream of the aluminium model. The local seeding system was constructed by covering a 0.05 m $\times$ 1 m slit in the wind tunnel wall with a large wooden box. On the inside of the tunnel, the slit was covered with an aluminium plate, with a regular arrangement of 2 mm circular holes, mounted flush to the side wall. The wooden box was connected to a conventional impactor seeding generator that creates Di-Ethyl-Hexyl-Sebacat (DEHS) particles with an approximately 1 µm mean diameter, (Kähler, Sammler & Kompenhans 2002). The box was filled with tracer particles, which are sucked through the aluminium grid into the boundary layer due to the reduced pressure in wind tunnel. This system is ideal for boundary layer experiments, as the seeding is fed directly into flow region of interest. Furthermore, the location and concentration of the tracer particles can be easily varied by adjusting the position and number of openings in the aluminium plate and the settings of the seeding generator. The disturbance to the flow is minimal as the particles are sucked out of the reservoir by means of the slightly lower pressure in the wind tunnel test section. Moreover, a homogeneous concentration of particles

https://doi.org/10.1017/jfm.2019.408 Published online by Cambridge University Press

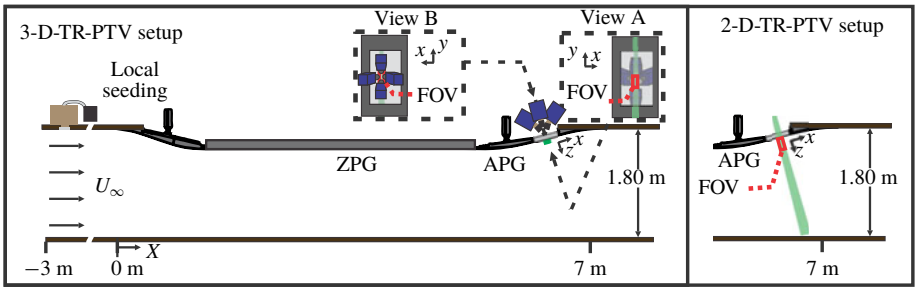


FIGURE 1. (Colour online) Top view of boundary layer model in the Atmospheric Wind Tunnel Munich (AWM) at the Bundeswehr University Munich and the two- and three-dimensional time-resolved particle tracking (2-D- and 3-D-TR-PTV) set-ups.

Parameter			3-D-TR-PTV	2-D-TR-PTV
Free-stream velocity	U_∞	(m s^{-1})	10	10
Friction *Re* end of ZPG	$Re_{\tau(ZPG)}$		5000	5000
Measurement location	X	(m)	6.25	6.30
Boundary layer thick	δ_{99}	(m)	0.185	0.195
Edge velocity at Meas. Location	U_f	(m s^{-1})	10	9.8
Displacement thick	δ^*	(m)	0.0262	0.0276
Momentum thick	θ	(m)	0.0161	0.0170
Pressure gradient	$\partial p/\partial x$	(Pa m^{-1})	44.5	42.8
	$\partial p/\partial x^+$		0.0235	0.0256
Clauser pressure grad. param.	β		13.5	14
Friction velocity	u_τ	(m s^{-1})	0.191	0.186
Wall unit	ν/u_τ	(μm)	79	80
Friction *Re*	Re_τ		2500	2400
Momentum thick *Re*	Re_θ		11 500	12 000
Wall shear rate	$\partial u/\partial z\|_{z=0}$	(s^{-1})	4300	4340

TABLE 1. The global boundary layer parameters, such as the incoming $Re_{\tau(ZPG)}$, δ_{99}, δ^*, θ and pressure gradient were measured in Reuther *et al.* (2015). The friction velocity u_τ and wall shear rate were directly measured in this investigation.

could be reached at the measurement location because of the natural turbulent mixing of the particles inside the boundary layer along the model, as discussed in Reuther & Kähler (2018) in detail.

The tracer particles in the APG region were illuminated in a wall-normal plane and a thin wall-parallel volume for the 2-D and 3-D configurations, respectively (see figure 1) by a continuous wave laser (Kvant Laser) with maximum output power of 8 W and 532 μm wavelength. For the volumetric measurement, the laser beam was formed into a uniform sheet of 40 mm width and thickness of approximately 1 mm and aligned directly adjacent to the wall. This beam profile was determined by using DataRay Inc. WinCamD-LCM1C beam profiling camera.

Time-resolved particle image sequences for the planar wall-normal PTV measurements were captured with 1 high-speed CMOS camera with 36 GB of RAM (Dimax-S4, PCO GmbH, LaVision) mounted on top of the wind tunnel to view the laser sheet perpendicularly, see figure 1. Using a 100 mm/f2.8 Makro-Planer Zeiss objective lens

https://doi.org/10.1017/jfm.2019.408 Published online by Cambridge University Press

Parameter			3-D-TR-PTV	2-D-TR-PTV
Recording rate	f	(Hz)	8200	7500
Time delay	Δt	(μs)	24	20
Resolution	m	(μm px^{-1})	25	26
Magnification	M		0.44	0.42
Field of view, FOV (3-D)	x, y, z	(mm^3)	$17 \times 25 \times 0.8$	—
	x, y, z	$[(\nu/u_\tau)^3]$	$200 \times 294 \times 9.5$	—
Field of view, FOV (2-D)	x, z	(mm^2)	—	7.5×30.3
	x, z	$[(\nu/u_\tau)^2]$	—	90×365
Image sequence.			$2 \times 55\,000$	$2 \times 55\,000$
Particle image per pixel	N_{ppp}		0.022	0.002

TABLE 2. Imaging parameters for particle tracking measurements. The coordinate system (x, y, z) corresponds to the streamwise, spanwise and wall-normal directions, respectively.

with a 2× tele-conversion lens, the resulting resolution in the centre of the field of view (FOV) was ∼26 μm px^{-1}. By dividing the pixel pitch of the high-speed camera (11 μm px^{-1}) the resulting magnification in the centre of the FOV was $M = 0.42$, corresponding to a field of view of 7.5 mm × 30.3 mm in the streamwise and wall-normal directions, respectively.

The 3-D time-resolved PTV measurements were captured with 4 high-speed CMOS cameras (Dimax-S4, PCO GmbH, LaVision) mounted in a 30° cross-configuration behind the glass viewing window in the APG, see figure 1. The coordinate system (x, y, z) defined in view A corresponds to the streamwise, spanwise and wall-normal directions respectively. Using 50 mm/f2.8 Makro-Planer Zeiss objective lenses and Scheimpflug mounts, the resulting resolution in the centre of the field of view (FOV) was ∼25 μm pix^{-1}. However, the resolution of the measurement is actually better as the particle images can be located with sub-pixel resolution (Kähler *et al.* 2012*a*,*b*). By dividing the pixel pitch of the HS camera the resulting magnification in the centre of the FOV was $M = 0.44$, corresponding to a field of view of 17 mm × 25 mm × 0.8 mm. The boundary layer thickness, determined from previous large field measurements at the measurement location, was $\delta_{99} \approx 190$ mm. An overview of the imaging parameters is given in table 2.

The evaluation of the data was performed with an in-house tomographic reconstruction method (Fuchs *et al.* 2016*a*, 2017) and time-resolved particle tracking methods described in Cierpka, Lütke & Kähler (2013*a*). For the 2-D imaging, a volume reconstruction was not necessary. Instead the 2-D locations of the particle images were identified using a Gaussian peak detection algorithm and then tracked using the aforementioned time-resolved methods. In contrast to PIV, particle tracking can greatly enhance the spatial resolution as spatial averaging over an interrogation window is avoided (Kähler *et al.* 2012*a*,*b*). Since near-wall flows typically feature very strong spatial gradients, especially when small vortices create reverse flow events, particle tracking is also advantageous as no bias errors due to spatial averaging over flow gradients takes place. However, reliable particle identification can be difficult for high seeding concentrations especially when the mean particle distance is much smaller than the mean displacements. Since modern high-speed cameras allow for the time-resolved sampling of the tracer particles, the temporal information was used to enhance the reliability and accuracy of the tracking procedure (Cierpka *et al.* 2013*a*; Kähler *et al.* 2016; Schanz *et al.* 2016).

https://doi.org/10.1017/jfm.2019.408 Published online by Cambridge University Press

After the particle image tracking, each found trajectory is then unambiguously identified by its common identification number and the algorithm estimates the velocity for each trajectory (particle positions in three dimensions and time) separately. The velocity estimation is based on a second-order polynomial fit of four consecutive positions. Taking the integral of the polynomial curve allows for a correction of the velocity estimation and compensation of bias errors due to curvature effects (Scharnowski & Kähler 2012). In addition, the vector position is reallocated and placed directly on the polynomial curve instead of in between the two positions as typically done in two-frame representations. This method is especially suited for the correct estimation of the velocity and vector position for trajectories with strong curvature (Cierpka *et al.* 2013*a*) as typical for the reverse flow events in the near-wall region of turbulent boundary layers (Bross & Kähler 2016; Schröder *et al.* 2016). However, if only two or three successive positions are known (i.e. end of a trajectory or short trajectories), the velocity estimation is based on the classical first-order displacement estimation and second-order vector positioning (Raffel *et al.* 2018).

3. Trajectory length and validation

The length of particle trajectories can be quite different depending on the particle velocity and where or when they enter or exit the measurement volume, see figure 2(*b*). In order to understand the distribution of trajectory lengths, a rectangular measurement volume with a uniform light intensity distribution can be considered, according to figure 2(*b*). It can be expected that the longest possible continuous tracks, like Track A, appear if a particle enters the volume right at the beginning of the image acquisition and disappear at the end of the volume during the image sequence. If the measurement time is sufficiently long, then the longest tracks are associated with particles that move close to the wall with a low velocity. Therefore, it follows that the faster the particles motion, the shorter the track length will be.

Short trajectories are also likely to appear at the boundaries of the measurement volume when particles locally enter the light volume due to the 3-D flow motion, see particles labelled B. In the present case, the probability of detecting short particle paths at the boundaries is quite large because of the thin extent of the volume in the wall-normal direction and the strong turbulent flow motion close to the wall. Short trajectories can also occur when two independent particle images overlap in the measurement volume due to crossing particle trajectories. This can cause a matching disparity during the volume reconstruction which will break longer tracks into separate tracks of smaller length, as shown by track C. This effect becomes more likely for a relatively dense seeding concentration inside the measurement volume. These points, in combination with spurious or miss-identified particle trajectories, explains the large detection rate of short trajectories, see figure 2(*a*). Therefore, in order to ensure that only correct trajectories are considered for the analysis, it is reasonable to use the track length as a detection criterion to remove valid but short particle tracks from the flow analysis.

To demonstrate the effect of applying a minimum trajectory length filter, the distributions of instantaneous and fluctuating streamwise velocity for different minimum trajectory lengths between 1 and 7 are plotted in figures 3(*a*) and 3(*b*). It is evident from these plots that changing the allowed minimum trajectory length influences the shape of the distribution. The maximum change, particularity in the far right and left tails, occurs between 1 and 3 minimum trajectory lengths. The distribution appears then to converge for minimum trajectory lengths from 4 to 7 for

https://doi.org/10.1017/jfm.2019.408 Published online by Cambridge University Press

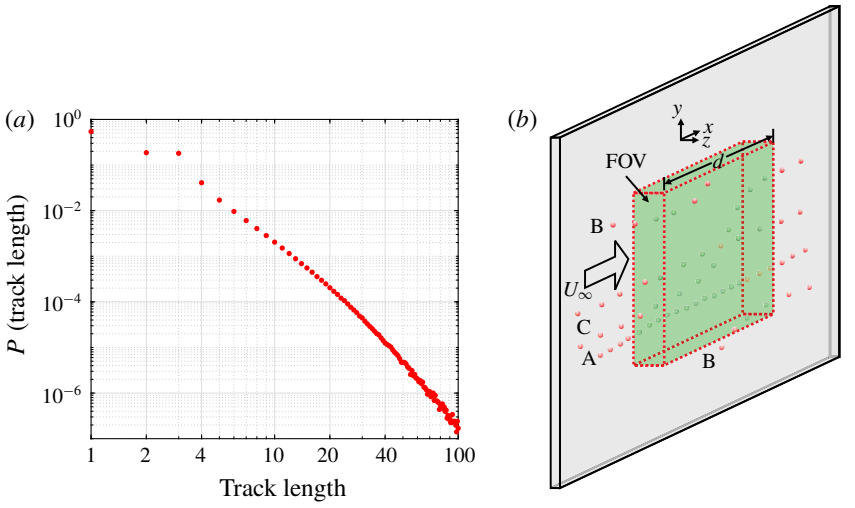


FIGURE 2. (Colour online) (*a*) Trajectory length probability. (*b*) Ideal laser sheet and trajectories.

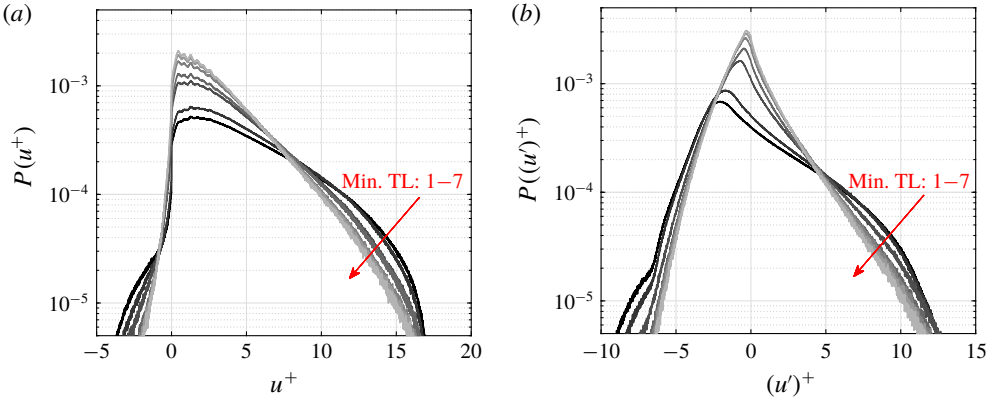


FIGURE 3. (Colour online) Probability distribution of (*a*) inner scaled streamwise velocity u^+ and (*b*) fluctuations $(u')^+$ for different minimum track lengths (Min TL) from 1 to 7.

both the instantaneous and fluctuating streamwise velocity in figures 3(*a*) and 3(*b*) respectively. Therefore, using a minimum trajectory length of 4 seems appropriate for use in the analysis presented in this paper. Another point to consider from this analysis is how the minimum trajectory length influences the percentage of reverse flow ($u^+ < 0$) detected. In figure 3(*a*) it appears that more reverse flow events are detected for decreasing minimum trajectory length. However, based on the discussion herein, this is due to outliers that appear as short trajectories. Furthermore, in this investigation a reverse flow event is defined as containing a minimum of two trajectories with $u < 0$ (further discussed in § 8). If this criterion is used the probability of reverse flow events with respect to the all detected trajectories remains constant (1.7 %), which means that the detection of reverse flow events in this paper is not influenced by the minimum trajectory length criterion.

https://doi.org/10.1017/jfm.2019.408 Published online by Cambridge University Press

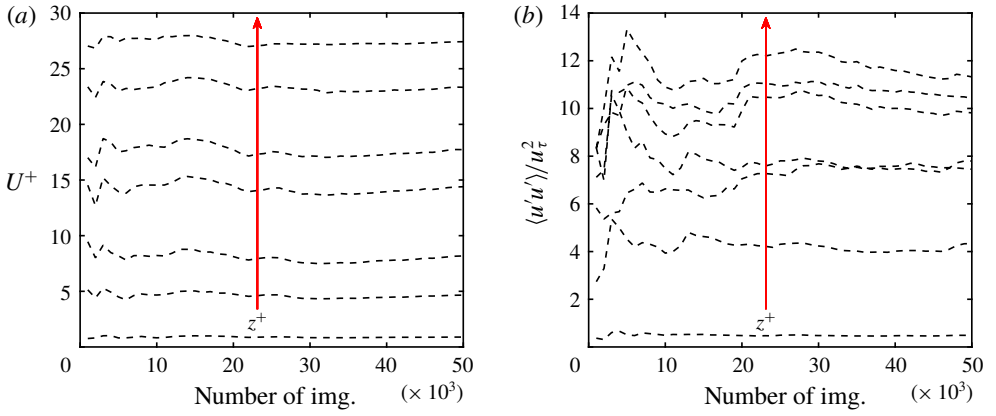


FIGURE 4. (Colour online) (*a*) Convergence of U^+ and (*b*) $\langle u'u' \rangle / u_\tau^2$ as functions of the number of sequential images used at wall-normal distances $z^+ = 1$, 5, 10, 50, 100, 200 and 300.

4. Mean field

In order to determine the proper inner scaling, the friction velocity, u_τ, has to be estimated from the slope of the mean velocity profile at the wall. The mean velocity profile was computed by sorting the trajectories into equally spaced bins in the z-direction and extending over the xy-planes. For the mean flow results, bins of z-direction spacing 25 μm and 12.5 μm were used for the 2-D and 3-D measurements, respectively. This bin spacing was selected so that sufficient data points appear within each bin. The number of samples in each bin not only depends on the homogeneity of the tracer particle distribution in the flow but also the number of images used to compute the mean statistics. To demonstrate that sufficient samples were used to calculate the mean statistics, the convergence of the mean streamwise velocity U^+ and $\langle u'u' \rangle / u_\tau^2$ as functions of the number of sequential image frames used at wall-normal distances $z^+ = 1$, 5, 10, 50, 100, 200 and 300 are plotted in figures 4(*a*) and 4(*b*). These plots demonstrate that the mean streamwise velocity is already well converged for all wall-normal locations at approximately 40 000 images. The fluctuations in figure 4(*b*) appear to require more than 50 000 samples to completely converge, especially in the log-law region. However, after 40 000 images the variation of the mean velocity fluctuations (figure 4*b*) with increasing number of images is less than 2 %.

The position of the wall is also important for the proper inner scaling and wall shear rate calculations, $\partial u / \partial z|_{z=0}$. In the 2-D measurement the orientation of the camera and the light sheet allows for the visualization of both the particle image and its reflection on the glass viewing window. The wall position is then calculated by applying the parallax correction method outlined in Cierpka, Scharnowski & Kähler (2013*b*) and Fuchs *et al.* (2018) for each particle–mirror image pair. For the 3-D measurement, the wall position is directly determined from the original camera calibration. For this experimental configuration a dual plane calibration target is placed directly on the window, which results in the $z = 0$ location of the reconstructed volume being at the wall position. This calibration procedure is only possible when the wind tunnel is not operating. Therefore, to account for any small shift in the wall position due to the negative pressure difference between the inside and outside of the test section,

https://doi.org/10.1017/jfm.2019.408 Published online by Cambridge University Press

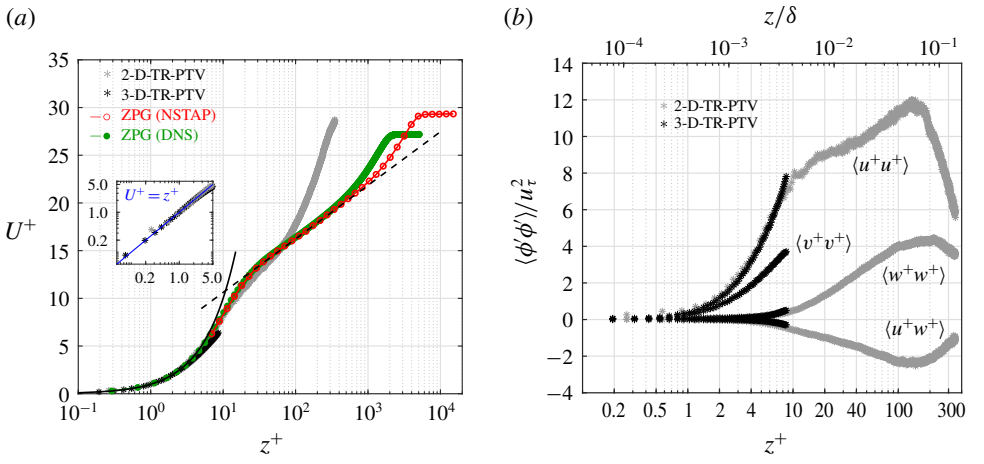


FIGURE 5. (Colour online) (*a*) Mean streamwise velocity U^+ and (*b*) Reynolds stress profiles versus wall-normal distances in viscous and outer scaling. In addition to the 2-D- and 3-D-TR-PTV data for an APG turbulent boundary layer at $Re_\tau \approx 2500$ ($Re_{\tau(ZPG)} = 5000$ in the preceding ZPG section) or $Re_\theta \approx 12\,000$ and Clauser pressure gradient parameters $\beta \approx 14$, nanoscale thermal anemometry probe (NSTAP) measurements at $Re_\tau = 6000$ (Samie *et al.* 2018) and DNS computations at $Re_\tau \approx 2000$ or $Re_\theta \approx 6500$ (Sillero, Jiménez & Moser 2013) of a ZPG turbulent boundary layer are plotted in (*a*). Also shown is the $U^+ = z^+$ indicated by the solid line and the dashed line represents $U^+ = \log(z^+)/0.41 + 5.0$.

the wall position can be confirmed in two other ways. First, the distribution of the reconstructed particle images in the z-direction clearly shows any shift in the wall location. Furthermore, a linear fit of the mean streamwise velocity profile will give a z-intercept corresponding to the correct wall position. Comparing the aforementioned methods made it possible to determine, with relative certainty, that the wall shifted a constant 0.05 mm during in all experiments presented herein.

Moreover, at the far edges of the measurement volume, the number of particles imaged will be limited due to the intensity profile of the laser. In these regions, the low number of particle images may have an effect on the statistical quantities due to outliers. Therefore, in all regions outliers are detected and removed and the mean value is calculated from a continuous distribution (Gauss fit) of the particle images in each bin. With this fit applied, the mean field in each bin can be calculated by either taking the peak of the Gauss fit or taking the mean of values within 2σ. For this investigation, velocities within 2σ of the fit applied to each bin were used to create the mean field and corresponding Reynolds Stress plots shown in figures 5(*a*) and 5(*b*), respectively.

Very good agreement between the 2-D- and 3-D-TR-PTV data sets for both the mean velocity and Reynolds stresses is seen in figures 5(*a*) and 5(*b*). Only for $z^+ > 8$ are the 3-D results slightly biased towards smaller velocities. This can be explained by taking into account two effects. First, the large displacements at the edge of the volume reduce the detection probability. In effect the detection of smaller velocities become more likely at the outer edge of the measurement volume. Second, the slightly elongated particle images in this faster moving region increase the reconstruction uncertainty in this region. In the forgoing sections, most of the analysis involving the 3-D data only considers the regions where $z^+ < 8$.

https://doi.org/10.1017/jfm.2019.408 Published online by Cambridge University Press

For this data set it appears that correct mean values were achieved for between $0.1 < z^+ < 8$ and $0.2 < z^+ < 310$ for the 3-D- and 2-D-TR-PTV data sets respectively. The standard deviation of the mean velocity values was estimated to be no larger than 0.05 m s^{-1}. Due to having reliable data points in the linear region ($U^+ = z^+$) of the turbulent boundary layer flow, calculating the viscous scaling is straightforward. A linear fit of $\bar{u}$ versus $\bar{z}$ in the region $1 < z^+ < 5$, where $u = \bar{u} + u'$ and $\bar{z}$ is the average bin position in the z-direction, allows for the calculation of $u_\tau = \sqrt{\nu\, \mathrm{d}\bar{u}/\mathrm{d}\bar{z}|_{z=0}}$ and the z-intercept indicates the wall location. Therefore, $U^+ = \bar{u}/u_\tau$, $u^+ = \bar{u}/u_\tau$ and $z^+ = zu_\tau/\nu$ can directly be calculated. The friction velocity was found to be $u_\tau = 0.191$ m s^{-1} which corresponds to a viscous length of $\nu/u_\tau = 79$ μm for the 3-D data set. Correspondingly, for the 2-D data set, $u_\tau = 0.186$ m s^{-1} and $\nu/u_\tau = 80$ μm. The suitability of the linear fit for the very near-wall region ($z^+ < 5$) is plotted in the zoomed-in inset in figure 5(*a*). To further corroborate the u_τ values calculated from this linear fit, a modified composite profile proposed for the inner scaled region proposed in Chauhan, Monkewitz & Hassan (2009) was applied to the 2-D-PTV data set for $z^+ = 0.1$–10. The resulting u_τ from this fit was 0.182, which is in good agreement with the value of 0.186 calculated by using a linear fit for $z^+ < 5$. In addition, the slight differences in these values for 2-D and 3-D sets can be explained by the slightly different streamwise measurement locations, see table 1. The standard deviation of the velocity and displacement for both data sets was estimated to be (in viscous units) 0.3 and 0.1 respectively.

In order to provide a point of reference for the 2-D- and 3-D-TR-PTV mean velocity and Reynolds stress profiles of an APG turbulent boundary layer at $Re_\tau \approx 2500$ (with $Re_{\tau(ZPG)} = 5000$ ZPG history) or $Re_\theta \approx$ 12 000 and Clauser pressure gradient parameter $\beta \approx 14$, NSTAP measurements at $Re_\tau = 6000$ (Samie *et al.* 2018) and DNS computations at $Re_\tau \approx 2000$ or $Re_\theta \approx 6500$ (Sillero *et al.* 2013) of a ZPG turbulent boundary layer are plotted in figure 5(*a*). This comparison shows that the viscous and buffer layers of the strong APG turbulent boundary layer overlay nicely with the ZPG cases when scaled with inner (+) units. However, the length of the log-law region significantly shortens for the APG flow when compared to the ZPG profiles. Another interesting feature of the strong APG flow is the presence of a large peak in $\langle u'u' \rangle$ located in the log-law layer or $z/\delta \approx 0.065$ in figure 5(*b*). In ZPG turbulent boundary layers the emergence of a secondary peak/plateau at large Reynolds numbers is widely documented (see § 1) and has been attributed to the presence of energetic superstructures residing in the log-law layer. To compare this observation further, the distribution of $\langle u'u' \rangle / u_\tau^2$ for the strong APG turbulent boundary layer in both inner and outer wall-normal direction scaling in comparison with ZPG profiles from the literature is plotted in figures 6(*a*) and 6(*b*). In agreement with the mean streamwise velocity profile, the strong APG streamwise Reynolds stress profiles measured with 2-D- and 3-D-TR-PTV agree well with ZPG DNS results of (Sillero *et al.* 2013) in the near-wall region when plotted with z^+ in figure 6(*a*). Furthermore, while the prominence of the inner peak for the strong APG is shadowed by the large secondary peak, the location of the inner peak remains rather fixed at $z^+ \approx 15$ for all the ZPG and APG cases. While the location of the outer peak/plateau moves outward in z^+ with increasing Reynolds number, the opposite trend occurs when scaling the wall-normal direction with the boundary layer thickness, see figure 6(*b*). In addition, it can also be observed that while a clearer secondary peak emerges for the highest Re_τ ZPG case plotted in figure 6(*b*), the height of the peak is still much lower than the strong APG case at a lower Reynolds number. This suggests that the superstructures associated with the secondary peak in turbulent boundary layers are

https://doi.org/10.1017/jfm.2019.408 Published online by Cambridge University Press

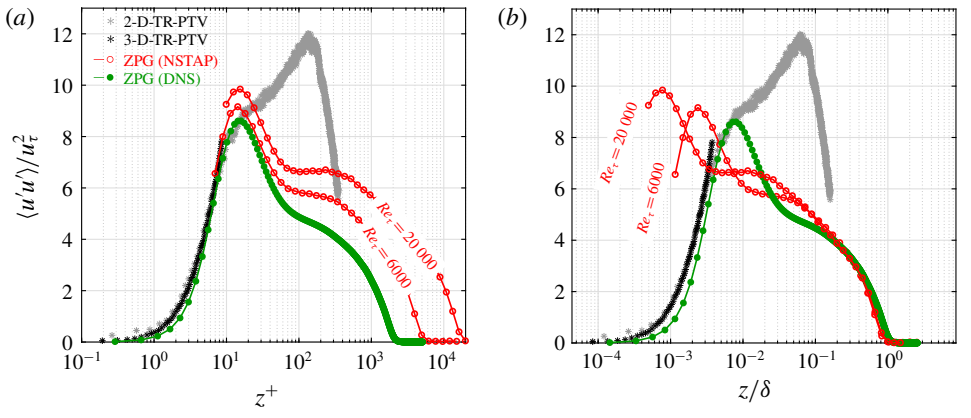


FIGURE 6. (Colour online) Mean streamwise Reynolds stress $\langle u'u'\rangle/u_\tau^2$ in (*a*) viscous and (*b*) outer wall-normal distance scaling. In addition to the 2-D- or 3-D-TR-PTV data for an APG turbulent boundary layer at $Re_\tau \approx 2500$ ($Re_{\tau(ZPG)} = 5000$ in the preceding ZPG section) and $Re_\theta \approx 12\,000$ and Clauser pressure gradient parameters $\beta \approx 14$, NSTAP measurements at $Re_\tau = 6000$ and 20 000 (Samie *et al.* 2018) and DNS computations at $Re_\tau \approx 2000$ or $Re_\theta \approx 6500$ (Sillero *et al.* 2013) of a ZPG turbulent boundary layer.

energized due to the presence of a strong adverse pressure gradient in a similar but more severe way as the effect of increasing the Reynolds number in ZPG turbulent boundary layers (Monty *et al.* 2011; Harun *et al.* 2013; Vinuesa *et al.* 2017*a*). It is also possible that the effect of the strong pressure gradient is to compress the streamwise length of the superstructures which results in a shrinking of the log-law layer observed in figure 5(*a*) and an increase in the height of the second energetic peak as observed in figures 6(*a*) and 6(*b*).

5. Flow field correlations

In this section the spatio-temporal connection between the flow structures in the viscous sublayer, buffer and log-law regions is examined using multi-point statistics. Using the time information in the recorded data, it is possible to make correlations in both space and time. These types of correlations have played an important role in the statistical analysis of temporal and spatial scales in turbulent flows, see Wallace (2014) and references therein. In the following section space–time correlations are calculated directly from a 2-D time-resolved data set using the following generalized form,

$$R_{\phi_i\phi_j}(x_0, z_0 + \Delta z, \Delta t) = \frac{\langle \phi_i(x_0, z_0, t_0)\phi_j(x_0, z_0 + \Delta z, t_0 + \Delta t)\rangle}{\sigma_{\phi_i(x_0,z_0,t_0)}\sigma_{\phi_j(x_0,z_0+\Delta z,t_0+\Delta t)}}, \tag{5.1}$$

where ϕ_i and ϕ_j $(i, j = 1, 2)$ are fluctuating velocity or wall shear stress, τ_W'. The location (x_0, z_0) is a point at a specific location in the streamwise and wall-normal directions that is then shifted in the wall-normal direction by Δz, and by incremental time steps $(t_0 + \Delta t)$. In other words the correlation is calculated by selecting a position and time series (x_0, z_0, t_0) and correlating that series for all other wall-normal locations, shifted in time by Δt. In the following correlation plots the vertical and horizontal axes are scaled in both inner and outer normalizations, i.e. $z^+ = zu_\tau/\nu$, z/δ, $t^+ = tu_\tau^2/\nu$ and tU_f/δ. Furthermore, the correlation calculation is made by averaging sub-samples

https://doi.org/10.1017/jfm.2019.408 Published online by Cambridge University Press

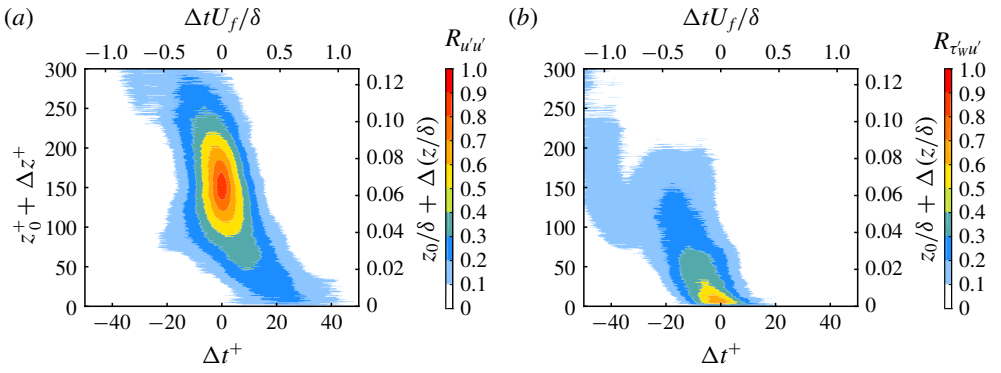


FIGURE 7. (Colour online) Space–time correlations (*a*) $R_{u'u'}$, where the starting point is at the outer peak location of the $\langle u'u' \rangle$ profile ($\sim z_0/\delta = 0.065$), and (*b*) $R_{\tau'_W u'}$, where τ'_W is the fluctuating wall shear stress, for an APG turbulent boundary layer at $Re_\tau = 2400$ ($Re_{\tau(ZPG)} = 5000$ in the preceding ZPG section) or $Re_\theta = 11\,500$, and Clauser pressure gradient parameter $\beta = 14$.

of the entire record time sequence which are approximately $tU_f/\delta = 300$ or $t^+ = 13\,000$ in length for each time record. The correlations in figures 7(*a*) and 7(*b*) are calculated for sub-sets of 1400 images corresponding to $\Delta t^+ = \pm 100$ or $\Delta tU_f/\delta = \pm 2.32$. For figure 7(*b*) the time shift is $\Delta t^+ = \pm 25$ or $\Delta tU_f/\delta = \pm 0.61$.

To begin this analysis, the auto-correlation of the streamwise velocity fluctuation u' at a starting point near the outer peak ($\sim z_0/\delta = 0.065$) is shown in figure 7(*a*). In this plot a strong positive correlation with almost no time shift within the log-law layer is visible. As the buffer and viscous layers are approached, the correlation shifts in the forward time direction. This phase shift means that it takes some time to detect the correlated flow motion at the wall compared to the location of the reference point. Therefore, this shift indicates forward leaning superstructures similar to the case of a ZPG turbulent boundary layer (Hutchins *et al.* 2011; Buchmann *et al.* 2016; Baars, Hutchins & Marusic 2017). More specifically, $R_{u'u'}$ values between 0.2 and 0.3 persist down to the wall and are positively shifted around $\Delta t^+ = 25$ or $\Delta tU_f/\delta = 0.6$. The correlation level implies that the near-wall field down to the viscous sublayer is strongly modulated by the flow dynamics in the buffer layer and log-law region in accordance with hot-wire measurements (Hutchins & Marusic 2007*b*; Mathis *et al.* 2009; Ganapathisubramani *et al.* 2012). Therefore, it can be concluded without any assumption that the flow motion in the viscous sublayer is modulated by small- and large-scale motions in the buffer and log-law region. The inclination angle of the large-scale motions, which is widely reported for ZPG flows in the range 12°–16° Adrian *et al.* (2000), Marusic & Heuer (2007), Baars *et al.* (2017), is not trivial for strong APG turbulent boundary layers due to the severely decelerating streamwise convection velocity of superstructures over the strongly curved APG model used in this investigation. However, direct numerical simulations of a self-similar APG turbulent boundary layer reported in Kitsios *et al.* (2017) show that the inclination angle of spatial correlations of $R_{u'u'}$ increases while the streamwise correlation length decreases for increasing APG compared to the ZPG case.

To evaluate the connection of the near and far fields in more detail, $R_{\tau'_W u'}$ was calculated and plotted in 7(*b*). As the correlation is positive, the results demonstrate that a high-momentum structure in the buffer layer and log-law region are associated

https://doi.org/10.1017/jfm.2019.408 Published online by Cambridge University Press

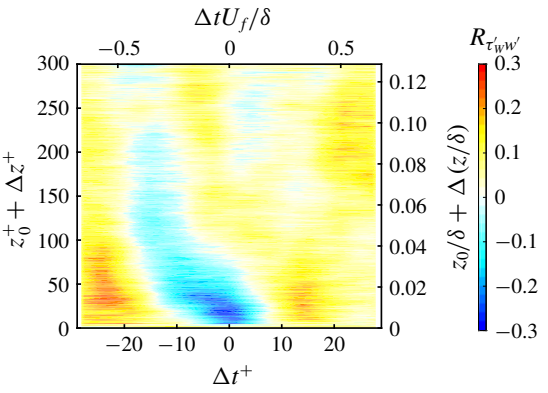


FIGURE 8. (Colour online) Space–time correlation $R_{\tau'_W w'}$, where τ'_W is the fluctuating wall shear stress and w' is the fluctuating wall-normal velocity, for an APG turbulent boundary layer at $Re_\tau = 2400$ ($Re_{\tau(ZPG)} = 5000$ in the preceding ZPG section) or $Re_\theta = 11\,500$, and Clauser pressure gradient parameter $\beta = 14$.

with a positive τ'_W and in turn also show that low-momentum structures are associated with a negative τ'_W at the wall. The shape of the correlation implies that a positive correlation in the wall-normal direction is skewed in the negative time direction. This means that the correlated signal at large wall distances had already passed the x-location when the corresponding signal is measured at the wall. The strong correlation signal above 0.6 between τ'_W and u' ends around the buffer layer but similarly to figure 7(*a*) there is a small correlation value extending into the log-law layer, which indicates the strong relationship between wall shear stress fluctuations and near-wall low-speed streaks. However, there is also a significant correlation between τ'_W and the log-law region which indicates that the turbulent superstructures manipulate τ'_W significantly.

Finally, with the readily available wall-normal velocity fluctuations w', the correlation of the wall shear stress and w' can be calculated and is plotted in figure 8. In this plot, a strong positive and negative correlation is visible. This shows that positive wall shear stress $\tau'_W > 0$ is associated with flow motion towards the wall and negative wall shear stress $\tau'_W < 0$ is correlated with motion moving away from the wall. This negative correlation of between -0.1 and -0.3 with negative time shift extends from the wall to the log layer. The maximum negative correlation appears at $(-0.85\Delta t^+,\ 17\Delta z^+)$. In addition, positive correlated regions in the near wall and buffer layer shifted by $\pm 20\Delta t^+$ on either side of the large negative correlated region show a different phase of the relationship between the wall shear stress and the wall-normal velocity. In these regions, negative wall shear stress is associated with flow towards the wall and positive wall shear stress is associated with flow away from the wall. In summary, the results of the direct measurements show that a strong relationship exists between the dynamics of the viscous sublayer and the flow motion in the buffer layer and log-law region.

6. Near-wall uniform-momentum zones

In this section it will be demonstrate that the flow near the wall can be classified into layers of uniform momentum. These regions have been studied and characterized

https://doi.org/10.1017/jfm.2019.408 Published online by Cambridge University Press

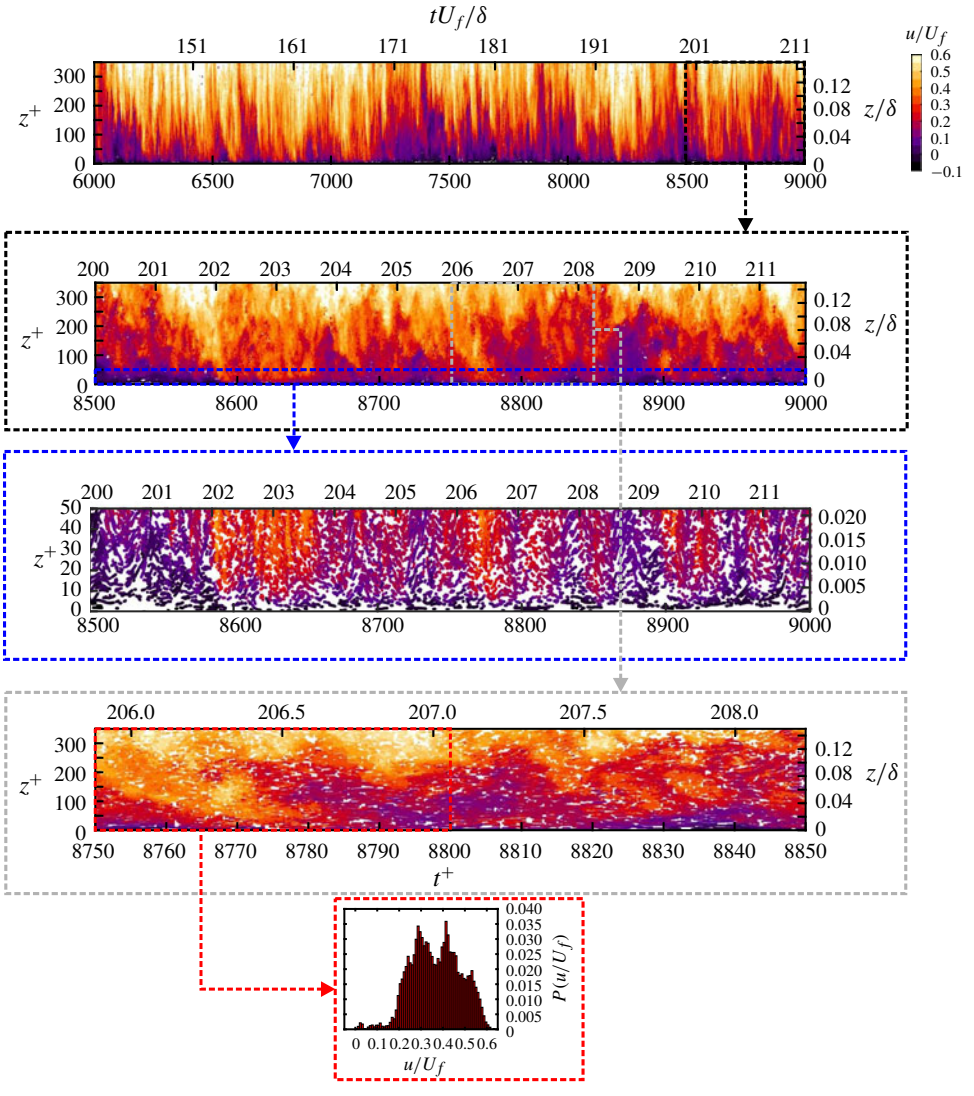


FIGURE 9. (Colour online) Time trace of trajectories coloured with u/U_f for an APG turbulent boundary layer at $Re_\tau = 2400$ ($Re_{\tau(ZPG)} = 5000$ in the preceding ZPG section) or $Re_\theta = 11\,500$, and Clauser pressure gradient parameter $\beta = 14$. In the top figure a space–time plot is made for $3000t^+$ or $70tU_f/\delta$, representing 10 500 recorded images. Smaller temporal selections are selected and plotted below the top figure.

for ZPG turbulent boundary layers in great detail by Meinhart & Adrian (1995), Adrian *et al.* (2000), de Silva *et al.* (2016), Laskari *et al.* (2018). However, none of these investigations resolved the near-wall flow features considered in this investigation. In this study, the velocity field in the lower log-law layer, buffer region and viscous sublayer are well resolved and therefore a brief analysis of the UMZs in the near-wall region is done.

In figure 9 trajectories are coloured with u/U_f, where the vertical axis is the wall-normal direction and time is plotted along the horizontal axis. In the top figure

https://doi.org/10.1017/jfm.2019.408 Published online by Cambridge University Press

a space–time plot is made for $3000t^+$ or $70tU_f/\delta$, representing 10 500 recorded images. Already in this representation several regions of similar momentum are visible due to the discreet colour bar. Furthermore, it can be seen that the UMZs appear frequently in time and their extent in the wall-normal direction and shape are also clearly visible from the visualization. However, since this view is compressed in the horizontal direction, smaller temporal selections are selected and plotted below the top figure to make the regions more visible. In each successive zoom in, the UMZs in the near-wall region become clearer. From visual inspection it seems that 2–3 UMZs are present in the near-wall region. To make the UMZ analysis more quantitative, a small number of trajectories were selected to create a probability density function (p.d.f.) of the instantaneous velocity, which is plotted in the bottom of figure 9. The p.d.f. was calculated for $50t^+$ or $1tU_f/\delta$, which is comparable when transformed into space via Taylor's frozen pattern hypothesis, to previous studies. Selecting a much larger region results in smoothing of the p.d.f. making the individual peaks of the UMZ not visible. In addition, the number of bins used for the histogram was 50, which was doubled and halved with no significant difference in the number of peaks identified. In this particular case, two or possibly three distinct peaks are detected. The peak locations and corresponding UMZ can be seen in the above trajectory plots by visual inspection. A movie showing the evolution of the near-wall UMZs can be found in the supplementary material available at https://doi.org/10.1017/jfm.2019.408 (movie 1).

The lowest UMZ is associated with the viscous sublayer, which is visible in the enhanced near-wall view (third from top) in figure 9. The low- and high-speed streaks in the buffer layer form another region of uniform momentum. The third layer is generated by low- and high-momentum superstructures. If we also consider flow regions that convect close to the mean flow velocity (see figure 10*a*) we can make a model that illustrates the possible layered UMZ combinations, see figure 10(*b*). In this model, representative superstructures and near-wall streaks in the buffer layer can be characterized by their streamwise velocity fluctuation magnitude relative to the local mean velocity. In figure 10(*b*), generalized near-wall streaks and superstructures with either (−)low- or (+)high-momentum are shown. In addition, fluid with momentum in between certain thresholds is designated as neutral in figure 10(*a*) or 0 in figure 10(*b*). This very general representation is based on the known coherent near-wall streaks and superstructures in the log-law layer. Using this representation of the near-wall and outer region structures, nine different combinations of structures can be made depending on how the superstructures in the log-law region and near-wall streaks and neutral flow are layered. Which means that in addition to the UMZ associated with the viscous sublayer, two additional UMZs with nine possible layering variations are expected based on this model. Therefore, the observation of 2–3 UMZs in figure 9 becomes understandable by taking the viscous sublayer into account. In previous studies, the average number of UMZs detected in ZPG turbulent boundary layers ranged from 3–5 depending on the Reynolds number (de Silva *et al.* 2016). It was also demonstrated that the number of detected UMZs is related to the passage of low- or high-momentum superstructures through the measurement plane and when these superstructures are connected with strong downward or upward motion ($Q4$ and $Q2$) the number of detected UMZs strongly decreases or increases (Laskari *et al.* 2018). In principle these findings show that the momentum of superstructures in the log-law layer and their footprint on the wall are strongly related to the number of instantaneous UMZs. This can also be generally explained by the different possible combinations superstructures layered on near-wall streaks shown in figure 10(*b*).

https://doi.org/10.1017/jfm.2019.408 Published online by Cambridge University Press

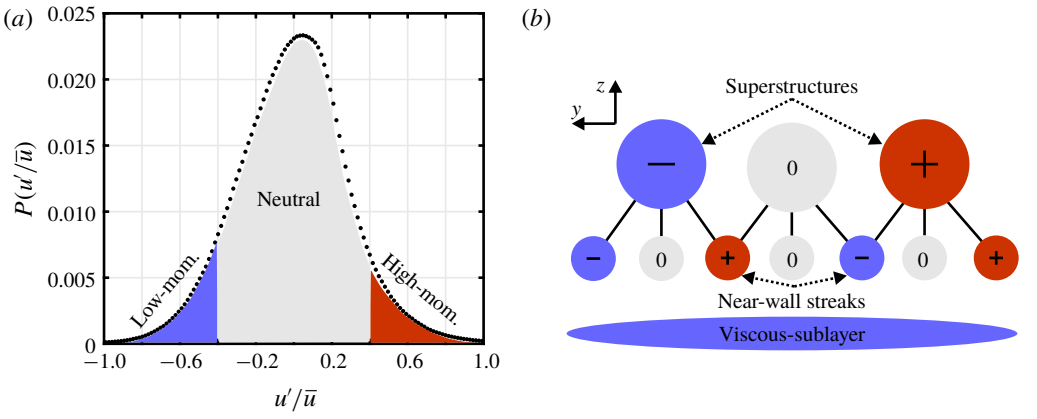


FIGURE 10. (Colour online) (*a*) Probability density function of $u'/\bar{u}$ for $z/\delta < 0.15$ with low-, neutral- and high-momentum regions highlighted. (*b*) Conceptual UMZs based on layering of low-, equal- or high-momentum superstructures and near-wall streaks above the viscous sublayer. The sign indicates the relative magnitude of the absolute velocity.

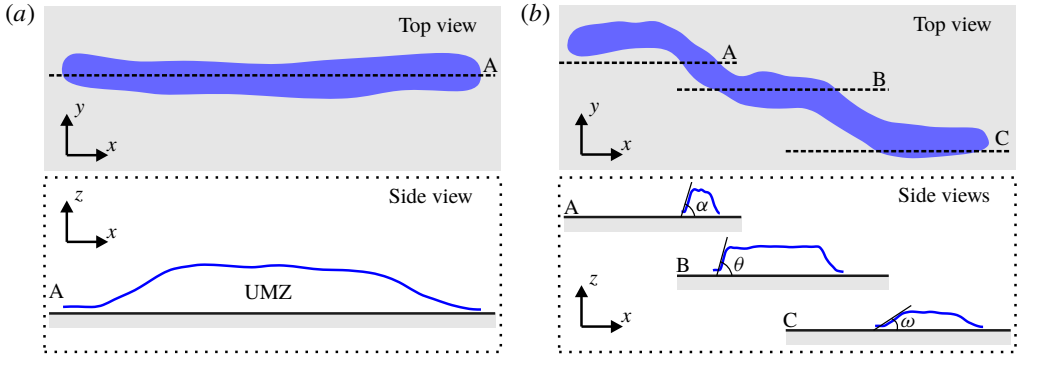


FIGURE 11. (Colour online) (*a*) Long streamwise oriented UMZ sliced by measurement plane A. (*b*) Meandering UMZ sliced by measurement planes A, B and C.

It is evident that these effects bias the length estimations of superstructures based on spatial correlation calculations towards smaller lengths.

The exact slope of the UMZ depends on how the meandering near-wall streaks are sliced by the measurement plane as indicated in figures 11(*a*) and 11(*b*). As the high-speed streaks are wider than the low-speed streaks (Jiménez, Del Álamo & Flores 2004; Lin *et al.* 2008) they dominate the specific UMZ in the measurement plane. However, when a low-speed streak passes through the measurement domain this is clearly visible. The flow in the log-law region is populated by turbulent superstructures of various lengths, heights and intensities which interact in a complex manner. In addition, the flow structures are faster in this region which makes their extent in the streamwise direction appear shorter. The typical slow layer structure with specific inclination angles becomes visible when a near-wall low-speed streak and a turbulent superstructure are sliced by the measurement plane, as shown in figure 11(*a*). However, due to the meandering nature of the structure shown in figure 11(*b*), they are often sliced by the measurement plane at different locations.

https://doi.org/10.1017/jfm.2019.408 Published online by Cambridge University Press

This leads to variations in length, heights and inclination angles of the UMZ in the side view. If the measurement plane slices through the structure in the middle like the A and B slices (see figure 11*b*), the inclination angle of the UMZ will be approximately the same, i.e. $\alpha \approx \theta$. However, when the measurement plane slices the structure on the side and not through the middle, see slice C in figure 11(*b*), the UMZ shown from the side will have a smaller inclination angle ω and consequently a shorter height than measured in slices A and B. This conceptual diagram illustrates how and when UMZs occur in the measurement plane, in terms of wall-normal and streamwise extents, inclination angle and temporal coherence.

This assessment of the UMZ in this section implies that at least 2–3 UMZs exist in the near-wall region. When considering the flow in the viscous sublayer, streaks in the buffer layer and superstructures in the log-law layer, this analysis is understandable. Therefore, it follows that different regions of uniform momentum form depending on the layering of the coherent structures which is sketched in a general form in figure 10(*b*). Consequently, the direct interaction between low- and high-speed streaks and superstructures is evident.

7. Space–time visualization

In the previous sections the strong correlation of the flow features in space and time was shown. However, the analysis does not allow for a distinction between low- and high-momentum flow structures. The positive correlation just states that if a velocity fluctuation is positive at a certain location it will be positive in the surrounding area. On the other hand if $u' < 0$, the surrounding correlation will also be positive. It is evident from the analysis of Buchmann *et al.* (2014) that the large-scale flow motions can significantly vary in their turbulent kinetic energy and it was also demonstrated that the slope of the correlated flow motion can be quite different depending on which structure is considered for the correlation. Therefore, in order to study how low- and high-momentum large-scale structures alter in time, a space–time plot of the streamwise fluctuation fields over a long time sequence was made, see figure 12.

This plot was made by selecting a thin wall-normal slice of the flow field and plotting all the trajectories passing through that slice with time. In the case of the wall-normal planar data (2-D-TR-PTV), trajectories passing through a thin (streamwise) strip extending from the wall to 350 viscous units over 45 000 image sequences, corresponding to temporal lengths of $t^+ = 12\,500$ or $tU_f/\delta = 293$, are plotted in figure 12. The trajectories are coloured with the streamwise fluctuating velocity, u', scaled with the local streamwise mean velocity, $\bar{u}$. A similar approach was used for ZPG turbulent boundary layers in Willert (2015).

The first things immediately visible in figure 12 are the intermittent low- ($u'/\bar{u} < 0$) and high- ($u'/\bar{u} > 0$) momentum regions. Since these data are compressed in order to show a long time sequence, these regions in the log layer are actually elongated structures in space. In accordance with the findings in § 5 these regions often go all the way down to the wall, which indicates that a low- or high-momentum structure is aligned with a corresponding low- or high-speed near-wall streak and the dynamics within the viscous sublayer, as already pointed out. Sometimes the regions only exist for $tU_f/\delta = 1$–2 and other times there are sustained low- or high-momentum regions that persist for more than $tU_f/\delta = 10$. A few examples of these short and sustained regions of low and high momentum are indicated in respective dashed boxes in figure 12. The strong variation of the length is caused by the meandering nature of the large-scale structures. If they are elongated in the streamwise direction a straight

https://doi.org/10.1017/jfm.2019.408 Published online by Cambridge University Press

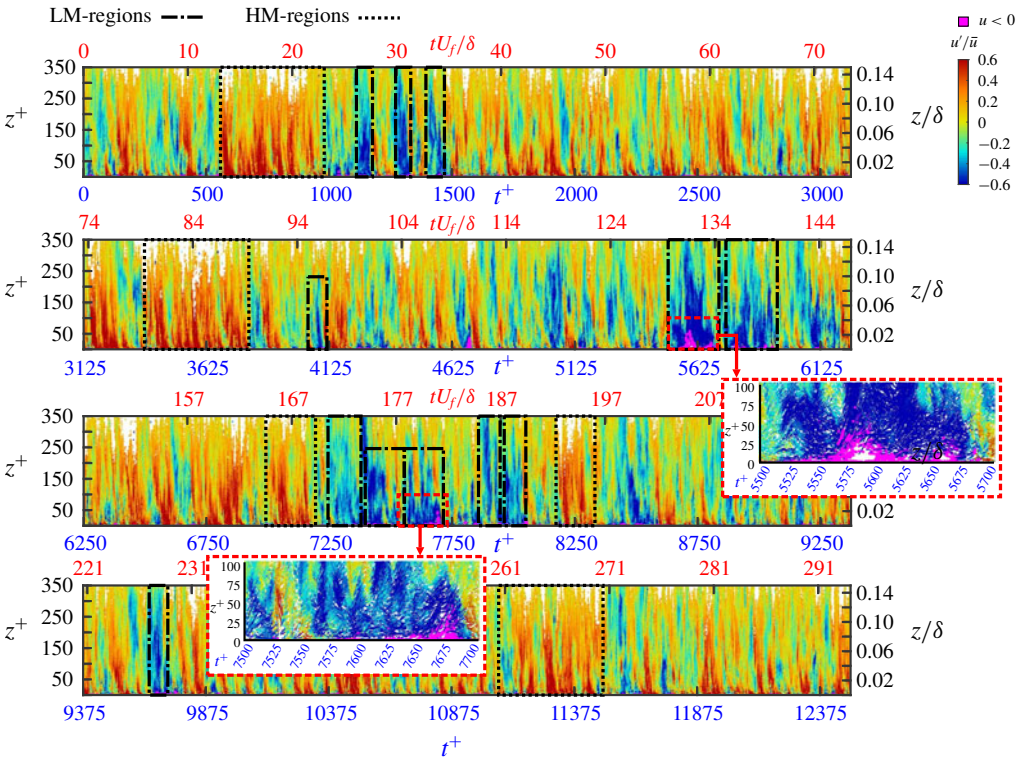


FIGURE 12. (Colour online) Space–time plot over $t^+ = 12\,500$ or $tU_f/\delta = 293$, from the 2-D data set coloured with $u'/\bar{u}$ where purple regions represent $u < 0$. Selected high-momentum (HM) and low-momentum (LM) regions are indicated in dashed boxes.

and long coherent signal can be observed, see figure 11(*a*). However, if the elongated structures are slightly curved they appear short in length in the measurement plane, see figure 11(*b*).

Also plotted in figure 12 are regions of reverse flow, in purple, where $u < 0$. The relatively sparse temporal distribution of the reverse flow events near the wall allows for the detection of such events by visual inspection. What is immediately evident is that reverse flow events only occur if a large region of surrounding flow is sufficiently retarded by a large-scale low-momentum flow structure (reverse flow events are always embedded in blue flow regions). If the near-wall flow is sufficiently retarded when a low-momentum superstructure interacts with a near-wall low-speed streak, the reverse flow events appear quite frequently. In all other situations, reverse flow events cannot be generated, which explains their rare occurrence. It also appears that the reverse flow events often appear in packages, i.e. multiple events right after each other once the conditions for reverse flow events are right.

Statistically, reverse flow regions appear relatively infrequently in time (around 1.7 %). In many cases the reverse flow events only exist for a short amount of time ($< 50t^+$) and remain close to the wall ($z^+ < 10$), e.g. at 1000–1500t^+. If the relative number of reverse flow events (with respect to the total number of $u < 0$) is calculated for each wall-normal location, almost 90 % of them occur below $z^+ = 10$ as shown in figure 13. Predictably, the locations where these reverse flow events occur coincide

https://doi.org/10.1017/jfm.2019.408 Published online by Cambridge University Press

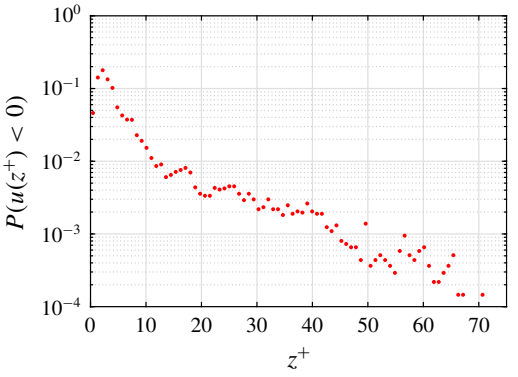


FIGURE 13. (Colour online) Relative number of reverse flow events ($u < 0$) at a given inner scaled wall-normal location (z^+) normalized by the total number of reverse flow events in an APG turbulent boundary layer at $Re_\tau = 2400$ ($Re_{\tau(ZPG)} = 5000$ in the preceding ZPG section) or $Re_\theta = 11\,500$, and Clauser pressure gradient parameter $\beta = 14$.

with regions of low momentum, as the flow must be sufficiently decelerated so that the flow reversal can happen.

However, there are instances where large or extreme reverse flow events appear that persist for more than $150t^+$ or $4–5tU_f/\delta$ and extend past $z^+ = 50$, e.g. $5500–5700t^+$ and $7500–7700t^+$. These improbable (according to figure 13) events are shown in a zoomed in view in figure 12. In these cases, a large decelerated region appears in the surrounding flow field and extends well into the buffer and log layer. The lifetime and spatial distribution of these decelerated flow regions can be explained again by the superposition of an elongated low-momentum large-scale structure convecting on a low-speed near-wall streak. Further evidence of this large-scale structure and streak layering is evidenced by the large regions of accelerated flow, e.g. $13–23tU_f/\delta$ and $79–89tU_f/\delta$, which can be explained by the superposition of a high-momentum large-scale structure on high-speed near-wall streaks. Therefore, it appears, based on figure 12, that under this superimposed condition large or extreme reverse flow events can take place in APG flow, which might lead to extended flow separation if the conditions are appropriate.

To examine this hypothesis in more detail, a 3-D measurement in the near-wall region was made. In the following discussion, near-wall features and the distribution of reverse flow events in the spanwise direction and how they are associated with the meandering near-wall streaks will be shown. As this information is embedded in the 3-D near-wall data set (3-D-TR-PTV), a corresponding space–time plot was made. In this case, trajectories passing through a wall-normal ($z^+ = 1–5$) and spanwise ($310y^+$) volume over a subset of the entire data set (20 000 image sequences or $4450t^+$ or $98tU_f/\delta$) is plotted in figure 14. The trajectories are coloured with the streamwise fluctuating velocity, u', scaled with the local streamwise mean velocity, $\bar{u}$. Reverse flow is indicated in purple where $u < 0$.

Directly visible in this plot are the low- and high-speed near-wall streaks and the locations of reverse flow events with respect to the streaky pattern. It appears in almost all the cases shown here that the reverse flow events occur inside or at the edge of a low-speed streak, a few of which are indicated in dashed ellipses in figure 14. Furthermore, it appears that when a reverse flow event appears in a low-speed streak,

https://doi.org/10.1017/jfm.2019.408 Published online by Cambridge University Press

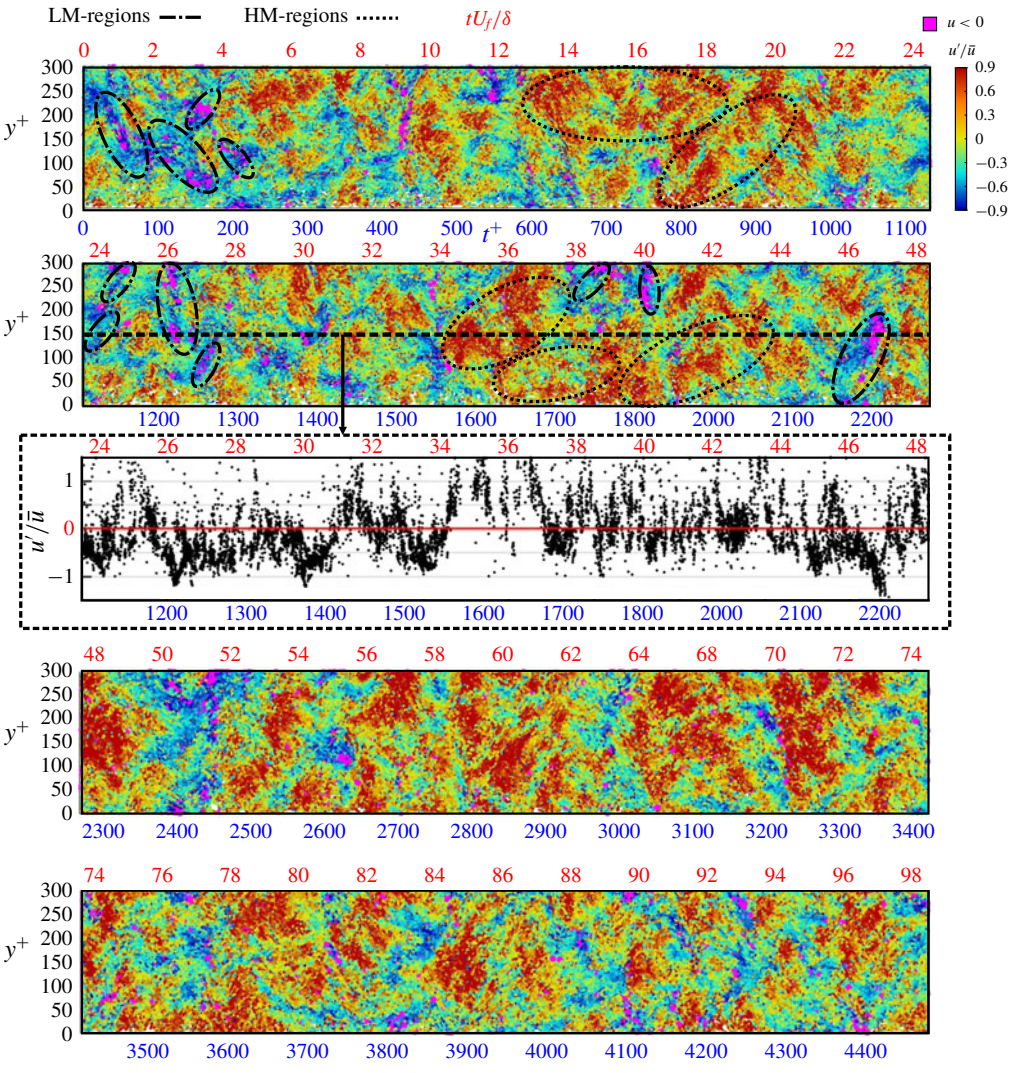


FIGURE 14. (Colour online) Space–time plot over $t^+ = 4450$ or $tU_f/\delta = 98$, from the 3-D data set coloured with $u'/\bar{u}$ where purple regions represent $u < 0$. Selected high-momentum (HM) and low-momentum (LM) regions are indicated in dashed ellipses.

that low-speed streak is often strongly tilted in the spanwise direction. This indicates the presence of streamwise oriented vortices that when slightly tilted, induce a slight flow reversal.

As observed in figure 12, in the near-wall topology there are sometimes regions of fast moving streaks that persist for 200–300t^+ or 6–8tU_f/δ (indicated in dashed ellipses). This can also be seen in the line plot of $u'/\bar{u}$ for a cut through the data at $y^+ = 150$. Although only the viscous sublayer and lower buffer layer are visualized there, this extended region of fast moving streaks is consistent with the lifetime of the superposition of large-scale structures and streaks shown in figure 12. What is also visible is the appearance of groupings for reverse flow events, distributed in the spanwise direction, e.g. between 0–250t^+ and 1150–1300t^+.

https://doi.org/10.1017/jfm.2019.408 Published online by Cambridge University Press

As established in figure 12, in order for these groupings to occur, the flow in the near-wall and far field regions must be sufficiently decelerated. This is achieved if a low-momentum large-scale structure is superimposed on a near-wall low-speed streak. In other words, groupings of reverse flow events can occur only when the flow is sufficiently decelerated by the layering of a low-speed near-wall streak and an elongated low-momentum large-scale structure in the far field. However, as this situation is often fulfilled, the question arises as to whether another event must take place simultaneously to make reverse flow events possible. A statistical analysis of these topological and dynamic features is provided in the next section.

8. Statistics of reverse flow events

8.1. *Reverse flow detection*

In the following sections a deeper statistical analysis of the reverse flow events is presented in order to quantitatively characterize their occurrence frequency, connection with other events and preferred orientation in the spanwise direction.

The probability of reverse flow events based on the distribution of the instantaneous streamwise velocity is shown in figure 15(*a*). In this plot the maximum probability occurs at a $u^+ = 1.5$ and sharply decreases in the $u^+ < 0$ region. In this case, the probability of reverse flow calculated by summing the region for $u^+ < 0$ or $\tau_W < 0$ in figure 15(*a*) or 15(*b*), is 0.017 or 1.7 %. This value represents a much larger value than presented in other measurements for a ZPG boundary layer and channel flow (Lenaers *et al.* 2012; Willert 2015; Willert *et al.* 2018). However, in the DNS channel flow computation in Lenaers *et al.* (2012), an increase in reverse flow probability for increasing Re_τ up to 1000 was reported. Furthermore, an increase in reverse flow probability was also reported for increasing APG conditions in Vinuesa *et al.* (2017*b*), which is intuitive as more flow reversal is expected as separation is approached. Therefore, the relatively large reverse flow measured herein at $Re_\tau = 2400$ ($Re_{\tau(ZPG)} = 5000$ in the preceding ZPG section) for a turbulent boundary layer with APG conditions is in accordance with the trends reported in the aforementioned DNS studies. However, different upstream pressure gradient development histories over a wing and an APG turbulent boundary layer (preceded by a long ZPG) at matched β can result in mean wake and Reynolds stresses differences (Bobke *et al.* 2017) and can also contribute to differences in reverse flow event statistics.

Nevertheless, we can conclude that the existence of reverse flow events is not a low Reynolds numbers effect as they also appear at the relatively high Reynolds number investigated herein. As the magnitude of the near-wall velocity fluctuations is associated with the rising intensity of the turbulent superstructures with Reynolds number, and the fact that the superstructures modulate the near-wall features according to figures 7(*a*), 7(*b*) and 8, the number of reverse flow events is expected to increase with increasing Reynolds number. However, due to the strong velocity gradient in the wall-normal direction, their extension in the in z-direction reduces, as shown in figure 13. This makes their measurement at large Reynolds number more difficult due to spatial resolution limitations. However, in the analysis all reverse flow events can be reliably resolved.

The low probability of reverse flow can also be illustrated by calculating the instantaneous wall shear stress. Taking advantage of the high spatial resolution in the viscous sublayer, the wall shear stress, $\tau_W = \mu \partial u/\partial z|_{z=0}$, can be directly calculated. The probability distribution function for the inner scaled wall shear stress is provided in figure 15(*b*) for completeness. This plot is more relevant than plot 15(*a*) as the

https://doi.org/10.1017/jfm.2019.408 Published online by Cambridge University Press

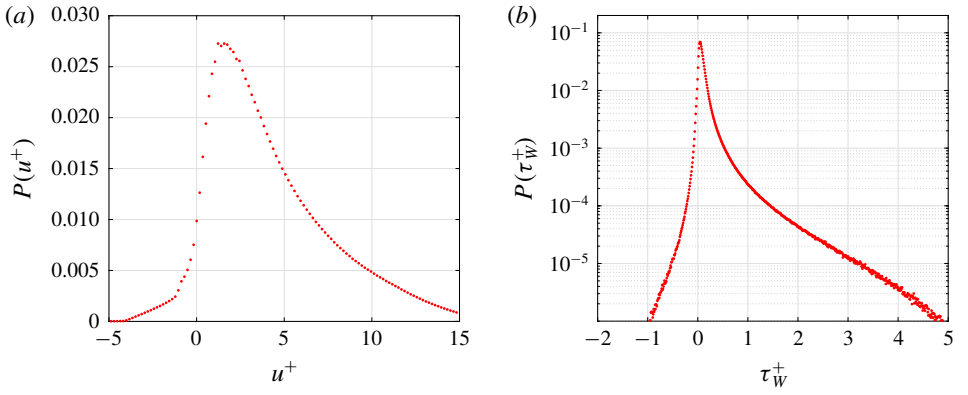


FIGURE 15. (Colour online) (*a*) Inner scaled instantaneous streamwise velocity (u^+) and (*b*) inner scaled instantaneous wall shear stress (τ_W) probabilities, from 3-D-TR-PTV measurements for $z^+ < 8$ in an APG turbulent boundary layer at $Re_\tau = 2500$ ($Re_{\tau(ZPG)} = 5000$ in the preceding ZPG section) or $Re_\theta = 12\,000$, and Clauser pressure gradient parameter $\beta = 13.5$.

distribution of the wall shear stress does not depend on the height of the measurement volume.

In the aforementioned discussion and figures the probability of individual reverse flow trajectories of tracer particles was considered. However, it must be kept in mind that a reverse flow event is comprised of many tracer particles and therefore the occurrence probability of a reverse flow event (one large event comprised of many tracer particles) is actually much smaller, as will be discussed in § 8.4.

8.2. *Reverse flow and extreme wall-normal events*

Another feature of the near-wall region worth studying is the connection between extreme flow events and a strong wall-normal velocity. These events, which are associated with the sweep ($u' > 0$, $w' < 0$ or $Q4$) and ejection ($u' < 0$, $w' > 0$ or $Q2$) of the near-wall streaks have been well documented and discussed in the literature (see review Wallace (2012)). In this section, the connection of extreme wall-normal fluctuations and the reverse flow will be explored in order to determine if there is a link between them. In figure 16(*a*) the probability density function of the instantaneous wall-normal velocity, w, normalized by the root mean square w_{rms} is shown. In this plot, the probability of fluctuations beyond $\pm 8w_{rms}$ is several orders of magnitude lower than their maximum and therefore events outside of this range will be referred to as extreme events.

To examine the connection of wall-normal fluctuations and reverse flow events a joint probability function (j.p.d.f.) of u/u_{rms} and w/w_{rms} is plotted in 16(*b*). In this figure it appears that there is not a strong correlation between extreme wall-normal events (beyond $\pm 8w_{rms}$) and reverse flow events ($u/u_{rms} < 0$), which is in agreement with DNS results at lower Reynolds number (Lenaers *et al.* 2012; Vinuesa *et al.* 2017*b*). This shows that reverse flow events are a typical feature of the flow that are not connected to extreme wall-normal events. Therefore, there must be another responsible reason for their low occurrence probability.

https://doi.org/10.1017/jfm.2019.408 Published online by Cambridge University Press

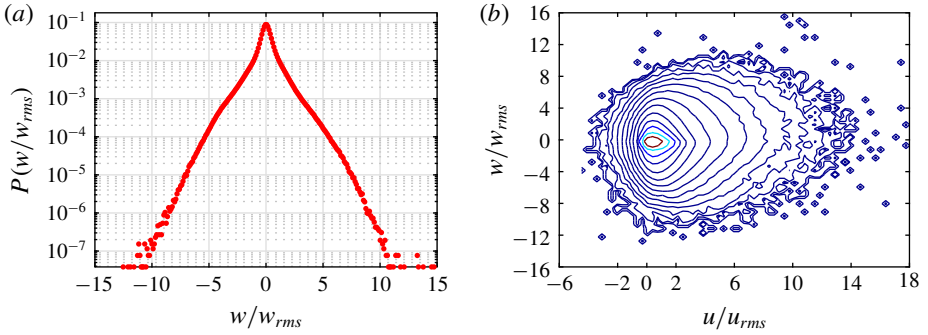


FIGURE 16. (Colour online) (*a*) Wall-normal fluctuation probability density function (p.d.f.) and (*b*) joint probability density function (j.p.d.f.) of wall-normal and streamwise velocities normalized with their root mean square.

8.3. *Flow direction statistics*

The previous analysis showed the characteristics of reverse flow events, i.e. their size, extent in the wall-normal direction and dynamics. Furthermore, it was shown that reverse flow events are not connected with extreme wall-normal events. Therefore, in this section the orientation of reverse flow motion is analysed; specifically their connection to spanwise motion, which could already be seen qualitatively in figure 14. To examine if there is a connection between reverse flow events and strong spanwise motion, the flow direction based on the u and v vector components (the wall-normal velocity component has little effect when compared to the other components) is calculated. In order to separate more extreme events the data set is conditioned into two groups with $|\tau_W| > \tau_{W,rms}$ and $|\tau_W| < \tau_{W,rms}$. The probability at each angle for each conditioned set is provided in figure 17. In these plots, 0° and 360° degrees indicate flow in the positive x-direction and 180° is flow purely in the negative x-direction. For each case the flow direction with the lowest probability was used to normalize the rest of the probabilities which are then scaled logarithmically. It must be noted that the conditioning requirement, $|\tau_W| > \tau_{W,rms}$, reduces the data set to only 35 % of the original set. Nonetheless, the preferred flow direction of these more intense events will provide insight into the larger turbulent action of the flow in the near-wall region.

In figure 17(*a*), where $|\tau_W| > \tau_{W,rms}$, the flow directions with the lowest probability occur at 90° and 270°, see figure 17(*a*). Relative to the probability at 90° and 270°, the flow is almost two orders of magnitude more likely to travel in the 180° direction. Therefore, it seems for these more intense fluctuations, the flow direction is most likely to have an upstream orientation during a reverse flow event. This was also seen in the DNS study for strong APG conditions in Vinuesa *et al.* (2017*b*). However, when looking at the other conditioned set of $|\tau_W| < \tau_{W,rms}$, which represents a much larger portion of the data set, a different distribution is present. In figure 17(*b*), the least likely probability occurs at 180° and the reverse flow for these fluctuations are more likely to have a strong spanwise component. This implies that reverse flow events of this type are associated with small streamwise vortex filaments that are close to the wall and slightly tilted with respect to the main flow direction.

Therefore, it becomes evident based the analysis in the previous sections that reverse flow events become possible if turbulent superstructures, near-wall low-speed

https://doi.org/10.1017/jfm.2019.408 Published online by Cambridge University Press

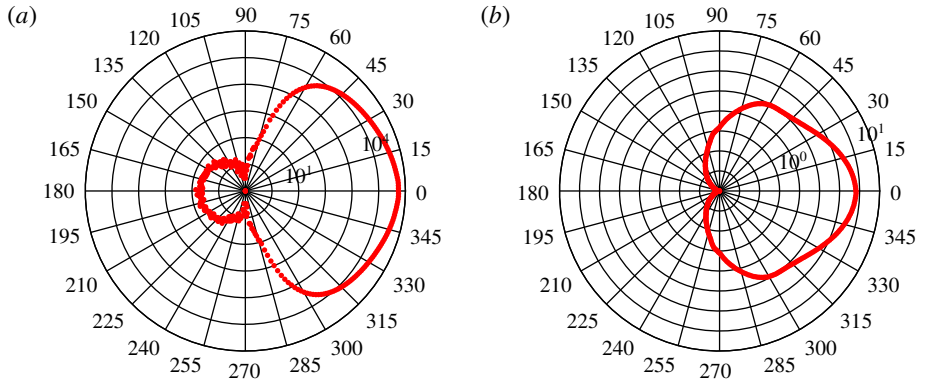


FIGURE 17. (Colour online) Logarithmically scaled flow direction probabilities for (*a*) $|\tau_W| > \tau_{W,rms}$ and (*b*) $|\tau_W| < \tau_{W,rms}$.

streaks and vortex filaments inside or near decelerated near-wall low-speed streaks interact in a specific manner. First, the low-speed streaks near the wall must be sufficiently retarded by low-momentum large-scale superstructure. Second, near-wall vortex filaments with the right attributes, i.e. distance to the wall and intensity, present in the vicinity of the retarded low-speed streaks, can cause reverse flow events. This complex interaction between the coherent flow motions explains why the reverse flow events are so rare.

8.4. *Reverse flow event lifetime*

According to the generation mechanism of reverse flow events outlined in the last section, it is understandable why these events are so rare. In this section the distribution and spacing of reverse flow events in time is addressed. Figure 18 shows the distribution of reverse flow events in time, where trajectories with $u < 0$ are grouped into bins of 50 time sequences.

Many intervals exist where almost no reverse flow events are detected. This is expected because when high-momentum large-scale structures convect through the measurement plane no events are possible according to the interaction model previously mentioned. Secondly, it appears that reverse flow events often appear in groups. This does not necessarily mean that they interact in these groups, but it seems that once a reverse flow event is detected, finding more events within a short time period is likely. This is evident from the model, i.e. when the right conditions are generated reverse flow event appearance becomes likely. By using analysis of this type, it is possible to locate image ranges where significant reverse flow occurs. Furthermore, if one considers the probability of major reverse flow events (bins with amplitudes larger than 2000), it is one order of magnitude less than previously calculated for individual reverse flow vectors, i.e. 0.1 % compared to 1.7 %. If the events seen in the 2-D data set are counted from figure 12 in this way, a similar percentage of 0.15 % of reverse flow events is measured.

The lifetime of large events is around 10–20 ms or $24t^+$ to $48t^+$ where $t^+ = (tu_\tau^2/\nu)$ but they can appear one after the other in a low-speed streak for up to and beyond 100 ms (or $240t^+$).

https://doi.org/10.1017/jfm.2019.408 Published online by Cambridge University Press

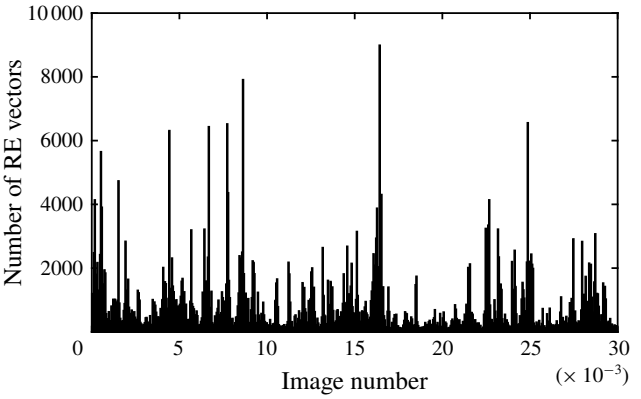


FIGURE 18. Reverse flow event detection over a time series, from 3-D-TR-PTV fields.

9. Reverse flow event visualization

In the following section, trajectory plots for a few of the extreme reverse flow events are provided. This is done to not only visualize the topology of these events but also further demonstrate the connection between reverse flow events and low-speed near-wall streaks, low-momentum superstructures and tilted longitudinal vortices.

In figure 19 a sequential set of flow trajectories during one of the large reverse flow events identified in figure 12 is shown in physical space with streamwise velocity colouring. In this case, each plot ($t1, t2, \ldots$) represents particle trajectories over 100 image sequences ($28.1t^+$). Highlighted in purple are reverse flow vectors. What can be seen in this sequence is the continued deceleration of the flow in the wall-normal direction (from $t1$ to $t3$) due the presence of a low-momentum superstructure, which sufficiently decelerates the near-wall flow allowing for the large flow reversal shown in plots $t4$ and $t5$. After this sequence of course the reverse bubble remains close to the wall (in $t6$ and $t7$) while the outer flow accelerates until the flow reversal disappears in $t9$. This would mean the convection velocity of this large reverse flow event bubble is around $0.5u^+$ which corresponds to a streamwise length of around 95 viscous units. This is longer than the average streamwise extension of reverse flow events of around $20x^+$ in Willert *et al.* (2018) for a ZPG turbulent boundary layer and in Vinuesa *et al.* (2017*b*) for turbulent flow over a wing, which is likely due to the fact that we are considering extreme events in a APG turbulent boundary layer. However, as indicated in figures 13 and 18, a variety of reverse flow events are detected in terms of their lifetime and extension in the wall-normal direction. Which suggests that a collection of reverse flow events exist in the strong APG flow considered in this investigation that have different convection velocities and sizes in the streamwise direction.

Furthermore, a selection of reverse flow events based on the maximum amplitude of the peaks in figure 18 are visualized in figure 20 by plotting three-dimensional trajectories coloured with $u'/\bar{u}$. With this colour coding, regions of low and high momentum with respect to the mean velocity can be quantitatively determined. Reverse flow, i.e. $u < 0$, is again highlighted in purple. A movie showing a short sequence of the three-dimensional near-wall flow can be found in the supplementary material (movie 2).

In figure 20(*a*) shows trajectories over a time series of 100 images ($28.4t^+$). Two views of the volume are shown, one in the xy plane and also a view looking at the

https://doi.org/10.1017/jfm.2019.408 Published online by Cambridge University Press

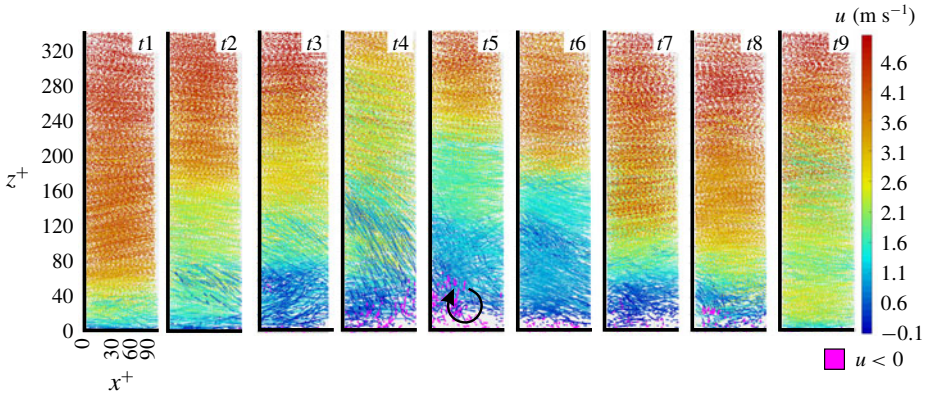


FIGURE 19. (Colour online) Two-dimensional trajectories during an extreme instantaneous reverse flow event in an APG turbulent boundary layer at $Re_\tau = 2400$ ($Re_{\tau(ZPG)} = 5000$ in the preceding ZPG section) or $Re_\theta = 11\,500$, and Clauser pressure gradient parameter $\beta = 14$. Trajectories are coloured with $u'/\bar{u}$, where positive flow is from left to right. Also highlighted are regions of $u < 0$. Each plot ($t1, t2, \ldots$) represents particle trajectories over 100 image sequences ($28.1t^+$).

volume from the left side of the xy plot in the zy plane. For this particular case, the streaky structure of low- and high-speed streaks is immediately obvious. Also visible are $u < 0$ events distributed in the regions of low speed. Looking at the xy view, these reverse flow events are present in a group in the near-wall low-speed streaks across the entire streamwise extent of the measurement volume, or approximately 150 viscous lengths. Moreover, the long streamwise extent of the low-speed streaks explains why the reverse flow events can be observed in packages.

To highlight that the topology of these reverse flow events is not universal as discussed in § 8.3, another set (independent of (*a*)) of instantaneous trajectories is plotted on the right, (*b*), side of figure 20. In contrast to (*a*), the flow is dominated by one large spanwise (y-direction) directed event. Trajectories with $u < 0$ appear grouped in a defined spatial location and extend over and area of 120×120 viscous lengths in the streamwise and spanwise directions, which is much larger than the spanwise extent of the low-speed streaks shown in (*a*). Furthermore, the significant spanwise motion of this flow event was not observed to this extent in (*a*).

Considering the results presented here, it is evident that the large spanwise motion must be associated with a slightly titled longitudinal vortex, as previously reported in Lenaers *et al.* (2012) and Diaz-Daniel *et al.* (2017). This is confirmed by the cross-plane visualization (zy view). If the axis of a streamwise vortex is slightly tilted with respect to the mean flow direction due to the meandering of the vortices, these longitudinal vortices can generate reverse flow events, provided the vortex travels with a sufficiently low convection velocity, which is possible when the vortex is sufficiently strong, located close to the wall and embedded inside a low-speed streak. Consequently, this generation mechanism is based on a interaction between low-speed streaks and tilted streamwise vortices. If the local convection velocity is increased locally by high-speed large-scale superstructures, reverse flow events are fully suppressed and cannot appear, as discussed in previous sections and shown in figures 12 and 14.

https://doi.org/10.1017/jfm.2019.408 Published online by Cambridge University Press

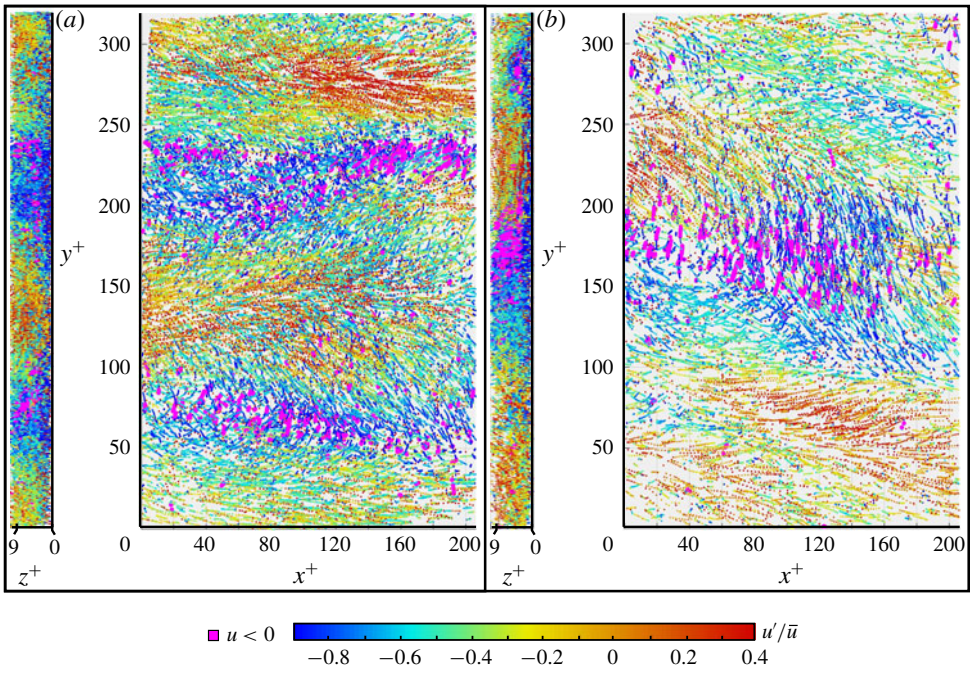


FIGURE 20. (Colour online) Three-dimensional trajectories during two different (*a* and *b*) instantaneous reverse flow events in an APG turbulent boundary layer at $Re_\tau = 2500$ ($Re_{\tau(ZPG)} = 5000$ in the preceding ZPG section) or $Re_\theta = 12\,000$, and Clauser pressure gradient parameter $\beta = 13.5$. Trajectories are coloured with $u'/\bar{u}$, where positive flow is from left to right. Also highlighted are regions of $u < 0$.

10. Concluding remarks

The work presented herein investigates the coherent flow motions in an adverse pressure gradient turbulent boundary layer following a zero pressure gradient turbulent boundary layer at $Re_\tau = 5000$ with a novel time-resolved volumetric PTV technique developed by the authors. This technique is able to determine with high spatial resolution, low uncertainty and without bias errors (due to spatial averaging for instance) the flow velocity within the buffer and viscous sublayer. Furthermore, time-resolved particle tracking measurements were performed in a single wall-normal slice in order to measure over long times the interaction of the turbulent superstructures with the near-wall flow motions down to the viscous sublayer.

Using the information in time and space, it was confirmed directly that the superstructures modulate the near-wall flow all the way down to the viscous sublayer. The modulation of the wall shear stress is therefore determined by the length, intensity and frequency of the superstructures and scales with outer units. The analysis of the space–time correlations show that the near-wall motion responds to the influence of the outer layer motion with a characteristic time shift. This is due to the forward leaning nature of the large-scale structures.

Due to the high spatial resolution of the measurements near the wall, characteristic uniform-momentum zones could be resolved in the viscous sublayer, throughout the buffer layer and up to the log-law region. Due to the fact that the near-wall streaks and the superstructures exist in low-, neutral- and high-momentum form, their

https://doi.org/10.1017/jfm.2019.408 Published online by Cambridge University Press

superposition can lead to various UMZ patterns or layering. Taking also into account that the height of the coherent structures varies the thickness of each UMZs layer can be quite different in space and time. Furthermore, as the coherent structures meander quite strongly, they appear with a characteristic tilt or as shear layers with a characteristic angle if the measurement plane slices the structures at an angle, which is usually the case in planar PIV/PTV experiments.

It was shown that the reverse events appear in a region of low-momentum fluid extending from the wall to the log layer for this strong adverse pressure gradient turbulent boundary layer. For turbulent channel or boundary layers with little or low pressure gradients, reverse flow events have only been reported close to the wall, $z^+ < 5$ (Lenaers *et al.* 2012; Willert 2015; Willert *et al.* 2018). Nevertheless, this illustrates that the deceleration of the near-wall low-speed streaks by low-momentum superstructures is very important for the generation of reverse flow events. Furthermore, if reverse flow events appear, they are often followed by a sequence of events because if a low-momentum superstructure decelerates a low-speed streak sufficiently the conditions are appropriate for the appearance of reverse flow events. However, if a high-momentum superstructure is present in the observation plane, reverse flow events cannot be detected. This explains why the reverse flow events appear often in 'packages' or in a sequence. In addition, it was observed that most of the reverse flow events remain below $z^+ = 10$. However, at least two extreme cases were observed where large reverse flow regions occurred over many times steps that penetrate into even the log-law layer. These large reverse flow events can extend in both spanwise and streamwise directions up to $\sim$100 viscous units, which is larger than the dimensions given in the literature for the ZPG case at lower Reynolds numbers. Which may suggest that reverse flow events might trigger large-scale flow separations if the conditions are appropriate.

It is evident from the analysis that low-speed streaks are a necessary condition for the existence of reverse flow events. Another necessary condition is the deceleration of the low-speed streak by low-momentum superstructures. However, this condition is realized quite often in the flow and therefore the question arises as to why the reverse flow events are seen so seldom. A detailed analysis of the measurements has shown evidence of small longitudinally oriented vortices generating spanwise directed trajectories in the vicinity of reverse events. The probability of the majority of reverse flow vectors having a significant spanwise component was shown to be much more likely than reverse events directed purely in the upstream direction, which is induced by the spanwise or wall-normal vortices. However, these kind of reverse flow events only occur when the axis of the streamwise vortices is slightly tilted with respect to the mean flow direction, generating flow in both the spanwise and upstream (reverse) directions.

The results clearly show that reverse flow events are not necessarily unique in terms of the topology and temporal frequency and it is evident that these differences are linked with the strength of the fluctuating near-wall flow. It was also demonstrated that reverse flow events are not strongly correlated with extreme wall-normal events, which perhaps provides further insight into dynamics of the near-wall flow. However, whenever the specific conditions are reached, i.e. sufficient deceleration of the near-wall low-speed streaks by low-momentum superstructures, multiple reverse flow events were shown to appear one after another if the interaction with a tiny near-wall vortex of sufficient strength takes place. Therefore, the following conceptual model, shown

https://doi.org/10.1017/jfm.2019.408 Published online by Cambridge University Press

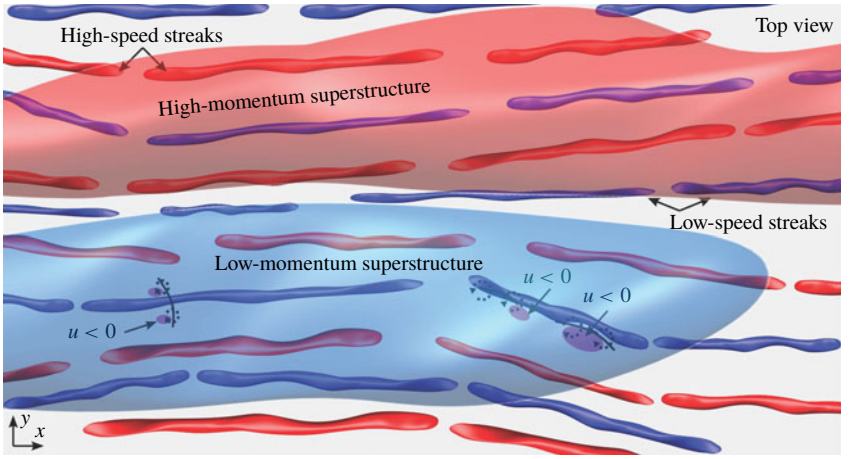


FIGURE 21. (Colour online) Conceptual model indicating the spatial distribution and interaction of coherent flow structures that lead to reverse flow events.

in figure 21, illustrates the possibility of reverse flow events based on the topological and statistical analysis presented herein.

(i) Low-speed near-wall streaks (dark blue) must be sufficiently decelerated by superimposed low-momentum large-scale superstructures (light blue).

(ii) Streamwise vortex filaments of sufficient intensity must be present at small wall distances and they must be located inside or near the retarded low-speed streaks to produce a sufficiently strong spanwise motion. When these particular vortices are slightly tilted with respect to the streamwise direction due to the meandering of the streaks for instance, they can produce reverse flow with a significant spanwise velocity component.

(iii) Spanwise vortices located at the retarded near-wall low-speed streaks can also produce reverse flow events but with a strong reverse flow component and only a small spanwise flow component.

(iv) The complex interaction of (i) and either (ii) or (iii) to generate reverse flow events explains why reverse flow events are quite rare. However, as (iii) is more dominant in high APG flows, reverse flow events become more common in these flows.

(v) If the near-wall flow is not strongly decelerated by low-momentum superstructures, reverse flow events are not possible. Which explains why there are large time intervals where no reverse flow events occur.

Acknowledgements

This work is supported by the Priority Programme SPP 1881 Turbulent Superstructures funded by the Deutsche Forschungsgemeinschaft project number KA1808/21-1.

Supplementary movies

Supplementary movies are available at https://doi.org/10.1017/jfm.2019.408.

https://doi.org/10.1017/jfm.2019.408 Published online by Cambridge University Press

REFERENCES

ADRIAN, R. J., MEINHART, C. D. & TOMKINS, C. D. 2000 Vortex organization in the outer region of the turbulent boundary layer. *J. Fluid Mech.* **422**, 1–54.

BAARS, W. J., HUTCHINS, N. & MARUSIC, I. 2017 Reynolds number trend of hierarchies and scale interactions in turbulent boundary layers. *Phil. Trans. R. Soc. Lond.* A **375** (2089), 1–18.

BALAKUMAR, B. J. & ADRIAN, R. J. 2007 Large- and very-large-scale motions in channel and boundary-layer flows. *Phil. Trans. R. Soc. Lond.* A **365** (1852), 665–681.

BOBKE, A., VINUESA, R., ÖRLÜ, R. & SCHLATTER, P. 2017 History effects and near equilibrium in adverse-pressure-gradient turbulent boundary layers. *J. Fluid Mech.* **820**, 667–692.

BROSS, M. & KÄHLER, C. J. 2016 Time-resolved 3D-PTV analysis of near wall reverse flow events in APG turbulent boundary layers. In *18th International Symposium on the App. of Laser and Imaging Tech. to Fluid Mech., July 4–7, Lisbon, Portugal*.

BRÜCKER, C. 2015 Evidence of rare backflow and skin-friction critical points in near-wall turbulence using micropillar imaging. *Phys. Fluids* **27** (3), 031705.

BUCHMANN, N.A., CIERPKA, C., KNOPP, T., SCHANZE, D., SCHRÖDER, A., HAIN, R. & KÄHLER, C.J. 2014 Large scale adverse pressure gradient turbulent boundary layer investigation by means of PIV and PTV. In *17th International Symposium on the App. of Laser and Imaging Tech. to Fluid Mech., July 7–10, Lisbon, Portugal*.

BUCHMANN, N. A., KÜCÜKOSMAN, Y. C., EHRENFRIED, K. & KÄHLER, C. J. 2016 Wall pressure signature in compressible turbulent boundary layers. In *Progress in Wall Turbulence 2*, pp. 93–102. Springer International Publishing.

CARDESA, J. I., MONTY, J., SORIA, J. & CHONG, M. 2014 Skin-friction critical points in wall-bounded flows. *J. Phys.* **506**, 012009.

CHAUHAN, K. A., MONKEWITZ, P. A. & HASSAN, H. N. 2009 Criteria for assessing experiments in zero pressure gradient boundary layers. *Fluid Dyn. Res.* **41** (2), 021404.

CHIN, C., VINUESA, R., ÖRLÜ, R., CARDESA, J.I., NOORANI, A., SCHLATTER, P. & CHONG, M.S. 2018 Flow topology of rare back flow events and critical points in turbulent channels and toroidal pipes. *J. Phys.* **1001**, 012002.

CIERPKA, C., LÜTKE, B. & KÄHLER, C. J. 2013*a* Higher order multi-frame particle tracking velocimetry. *Exp. Fluids* **54**, 1533.

CIERPKA, C., SCHARNOWSKI, S. & KÄHLER, C. J. 2013*b* Parallax correction for precise near-wall flow investigations using particle imaging. *Appl. Opt.* **52** (12), 2923–2931.

DIAZ-DANIEL, C., LAIZET, S. & VASSILICOS, J. C. 2017 Wall shear stress fluctuations: mixed scaling and their effects on velocity fluctuations in a turbulent boundary layer. *Phys. Fluids* **29** (5), 055102.

FERNHOLZ, H. H. & FINLEY, P. J. 1996 The incompressible zero-pressure-gradient turbulent boundary layer: an assessment of the data. *Prog. Aerosp. Sci.* **32** (4), 245–311.

FUCHS, T., BROSS, M., SCHARNOWSKI, S. & KÄHLER, C. J. 2018 Parallax corrected PTV for precise near wall boundary layer measurements. In *19th International Symposium on the App. of Laser and Imaging Tech. to Fluid Mech., July 16–19, Lisbon, Portugal*.

FUCHS, T., HAIN, R. & KÄHLER, C. J. 2016*a* Double-frame 3D-PTV using a tomographic predictor. *Exp. Fluids* **57**, 174.

FUCHS, T., HAIN, R. & KÄHLER, C. J. 2016*b* Uncertainty quantification of three-dimensional velocimetry techniques for small measurement depths. *Exp. Fluids* **57**, 73.

FUCHS, T., HAIN, R. & KÄHLER, C. J. 2017 Non-iterative double-frame 2D/3D particle tracking velocimetry. *Exp. Fluids* **58**, 119.

GANAPATHISUBRAMANI, B., HUTCHINS, N., HAMBLETON, W. T., LONGMIRE, E. K. & MARUSIC, I. 2005 Investigation of large-scale coherence in a turbulent boundary layer using two-point correlations. *J. Fluid Mech.* **524**, 57–80.

GANAPATHISUBRAMANI, B., HUTCHINS, N., MONTY, J. P., CHUNG, D. & MARUSIC, I. 2012 Amplitude and frequency modulation in wall turbulence. *J. Fluid Mech.* **712**, 61–91.

HARUN, Z., MONTY, J. P., MATHIS, R. & MARUSIC, I. 2013 Pressure gradient effects on the large-scale structure of turbulent boundary layers. *J. Fluid Mech.* **715**, 477–498.

HUTCHINS, N. & MARUSIC, I. 2007*a* Evidence of very long meandering features in the logarithmic region of turbulent boundary layers. *J. Fluid Mech.* **579**, 1–29.

https://doi.org/10.1017/jfm.2019.408 Published online by Cambridge University Press

HUTCHINS, N. & MARUSIC, I. 2007*b* Large-scale influences in near-wall turbulence. *Phil. Trans. R. Soc. Lond.* A **365**, 647–664.

HUTCHINS, N., MONTY, J. P., GANAPATHISUBRAMANI, B., NG, H. C. H. & MARUSIC, I. 2011 Three-dimensional conditional structure of a high-Reynolds-number turbulent boundary layer. *J. Fluid Mech.* **673**, 255–285.

HUTCHINS, N., NICKELS, T. B., MARUSIC, I. & CHONG, M. S. 2009 Hot-wire spatial resolution issues in wall-bounded turbulence. *J. Fluid Mech.* **635**, 103–136.

JALALABADI, R. & SUNG, H. J. 2018 Influence of backflow on skin friction in turbulent pipe flow. *Phys. Fluids* **30** (6), 065104.

JIMÉNEZ, J., DEL ÁLAMO, J. C. & FLORES, O. 2004 The large-scale dynamics of near-wall turbulence. *J. Fluid Mech.* **505**, 179–199.

KÄHLER, C. J., ASTARITA, T., VLACHOS, P., SAKAKIBARA, J., HAIN, R., DISCETTI, S., LA FOY, R. & CIERPKA, C. 2016 Main results of the 4th international PIV challenge. *Exp. Fluids* **57**, 97.

KÄHLER, C. J., SAMMLER, B. & KOMPENHANS, J. 2002 Generation and control of tracer particles for optical flow investigations in air. *Exp. Fluids* **33**, 736.

KÄHLER, C. J., SCHARNOWSKI, S. & CIERPKA, C. 2012*a* On the resolution limit of digital particle image velocimetry. *Exp. Fluids* **52**, 1629.

KÄHLER, C. J., SCHARNOWSKI, S. & CIERPKA, C. 2012*b* On the uncertainty of digital PIV and PTV near walls. *Exp. Fluids* **52**, 1641.

KITSIOS, V., SEKIMOTO, A., ATKINSON, C., SILLERO, J. A., BORRELL, G., GUNGOR, A. G., JIMÉNEZ, J. & SORIA, J. 2017 Direct numerical simulation of a self-similar adverse pressure gradient turbulent boundary layer at the verge of separation. *J. Fluid Mech.* **829**, 392–419.

KLEBANOFF, P. S. 1955 Characteristics of turbulence in a boundary layer with zero pressure gradient. *NASA Tech. Rep.* 1247 available from NASA, Washington, D.C.

KLINE, S. J., REYNOLDS, W. C., SCHRAUB, F. A. & RUNSTADLER, P. W. 1967 The structure of turbulent boundary layers. *J. Fluid Mech.* **30**, 741–773.

KNOPP, T., BUCHMANN, N. A., SCHANZ, D., EISFELD, B., CIERPKA, C., HAIN, R., SCHRÖDER, A. & KÄHLER, C. J. 2015 Investigation of scaling laws in a turbulent boundary layer flow with adverse pressure gradient using PIV. *J. Turbul.* **16** (3), 250–272.

KOVASZNAY, L. S. G., KIBENS, V. & BLACKWELDER, R. F. 1970 Large-scale motion in the intermittent region of a turbulent boundary layer. *J. Fluid Mech.* **41** (2), 283–325.

LASKARI, A., DE KAT, R., HEARST, R. J. & GANAPATHISUBRAMANI, B. 2018 Time evolution of uniform momentum zones in a turbulent boundary layer. *J. Fluid Mech.* **842**, 554–590.

LENAERS, P., LI, Q., BRETHOUWER, G., SCHLATTER, P. & ÖRLÜ, R. 2012 Rare backflow and extreme wall-normal velocity fluctuations in near-wall turbulence. *Phys. Fluids* **24** (3), 035110.

LIN, J., LAVAL, J. P., FOUCAUT, J. M. & STANISLAS, M. 2008 Quantitative characterization of coherent structures in the buffer layer of near-wall turbulence. Part 1. Streaks. *Exp. Fluids* **45**, 999.

MACIEL, Y., WEI, T., GUNGOR, A. G. & SIMENS, M. P. 2018 Outer scales and parameters of adverse-pressure-gradient turbulent boundary layers. *J. Fluid Mech.* **844**, 5–35.

MARUSIC, I. & HEUER, W. D. C. 2007 Reynolds number invariance of the structure inclination angle in wall turbulence. *Phys. Rev. Lett.* **99**, 114504.

MATHIS, R., HUTCHINS, N. & MARUSIC, I. 2009 Large scale amplitude modulation of the small scale structures in turbulent boundary layers. *J. Fluid Mech.* **628**, 311–337.

MEINHART, C. D. & ADRIAN, R. J. 1995 On the existence of uniform momentum zones in a turbulent boundary layer. *Phys. Fluids* **7**, 694–696.

MICHAEL, M. & RAINER, F. 2002 DNS of a turbulent boundary layer with separation. *Intl J. Heat Fluid Flow* **23** (5), 572–581.

MONTY, J. P., HARUN, Z. & MARUSIC, I. 2011 A parametric study of adverse pressure gradient turbulent boundary layers. *Intl J. Heat Fluid Flow* **32**, 575–585.

MONTY, J. P., HUTCHINS, N., NG, H. C. H., MARUSIC, I. & CHONG, M. S. 2009 A comparison of turbulent pipe, channel and boundary layer flows. *J. Fluid Mech.* **632**, 431–442.

NOVARA, M., SCHANZ, D., REUTHER, N., KÄHLER, C. J. & SCHRÖDER, A. 2016 Lagrangian 3D particle tracking in high-speed flows: Shake-The-Box for multi-pulse systems. *Exp. Fluids* **57**, 128.

https://doi.org/10.1017/jfm.2019.408 Published online by Cambridge University Press

RAFFEL, M., WILLERT, C., SCARANO, F., KÄHLER, C. J., WERELEY, S. T. & KOMPENHANS, J. 2018 *Particle Image Velocimetry. A Practical Guide*. Springer.

RAO, K., NARASIMHA, R. & NARAYANAN, M. 1971 The 'bursting' phenomenon in a turbulent boundary layer. *J. Fluid Mech.* **48**, 339–352.

REUTHER, N. & KÄHLER, C. J. 2018 Evaluation of large-scale turbulent/non-turbulent interface detection methods for wall-bounded flows. *Exp. Fluids* **59**, 121.

REUTHER, N., SCHARNOWSKI, S., HAIN, R., SCHANZ, D., SCHRÖDER, A. & KÄHLER, C. J. 2015 Experimental investigation of adverse pressure gradient turbulent boundary layers by means of large-scale PIV. In *11th International Symposium on PIV, September 14–16, Santa Barbara, USA*.

SAMIE, M., MARUSIC, I., HUTCHINS, N., FU, M. K., FAN, Y., HULTMARK, M. & SMITS, A. J. 2018 Fully resolved measurements of turbulent boundary layer flows up to $Re_\tau = 20\,000$. *J. Fluid Mech.* **851**, 391–415.

SAXTON-FOX, T. & MCKEON, B. J. 2017 Coherent structures, uniform momentum zones and the streamwise energy spectrum in wall-bounded turbulent flows. *J. Fluid Mech.* **826**, R6.

SCHANZ, D., GESEMANN, S. & SCHRÖDER, A. 2016 Shake-The-Box: Lagrangian particle tracking at high particle image densities. *Exp. Fluids* **57**, 70.

SCHARNOWSKI, S. & KÄHLER, C. J. 2012 On the effect of curved streamlines on the accuracy of PIV vector fields. *Exp. Fluids* **54**, 1435.

SCHRÖDER, A., SCHANZ, D., GEISLER, R. & GESEMANN, S. 2016 Investigations of coherent structures in near-wall turbulence and large wall-shear stress events using Shake-The-Box. In *18th International Symposium on the App. of Laser and Imaging Tech. to F. Mech., July 4–7, Lisbon, Portugal*.

SILLERO, J. A., JIMÉNEZ, J. & MOSER, R. D. 2013 One-point statistics for turbulent wall-bounded flows at Reynolds numbers up to $\delta^+ \approx 2000$. *Phys. Fluids* **25** (10), 105102.

DE SILVA, C. M., HUTCHINS, N. & MARUSIC, I. 2016 Uniform momentum zones in turbulent boundary layers. *J. Fluid Mech.* **786**, 309–331.

DE SILVA, C. M., PHILIP, J., HUTCHINS, N. & MARUSIC, I. 2017 Interfaces of uniform momentum zones in turbulent boundary layers. *J. Fluid Mech.* **820**, 451–478.

SIMPSON, R. L. 1989 Turbulent boundary layer seperation. *Annu. Rev. Fluid Mech.* **21**, 205–234.

SKÅRE, P. & KROGSTAD, P. 1994 A turbulent equilibrium boundary layer near separation. *J. Fluid Mech.* **272**, 319–348.

SMITH, C. R. & METZLER, S. P. 1983 The characteristics of low-speed streaks in the near-wall region of a turbulent boundary layer. *J. Fluid Mech.* **129**, 27–54.

SPALART, P. R. & COLEMAN, G. N. 1997 Numerical study of separation bubble with heat transfer. *Eur. J. Mech. (B/Fluids)* **16**, 169–187.

VALLIKIVI, M., HULTMARK, M. & SMITS, A. J. 2015 Turbulent boundary layer statistics at very high Reynolds number. *J. Fluid Mech.* **779**, 371–389.

VINUESA, R., HOSSEINI, S. M., HANIFI, A., HENNINGSON, D. S. & SCHLATTER, P. 2017*a* Pressure-gradient turbulent boundary layers developing around a wing section. *Flow Turbul. Combust.* **99** (3), 613–641.

VINUESA, R., ÖRLÜ, R. & SCHLATTER, P. 2017*b* Characterisation of backflow events over a wing section. *J. Turbul.* **18**, 170–185.

WALLACE, J. M. 2012 Highlights from 50 years of turbulent boundary layer research. *J. Turbul.* **13**, 1–70.

WALLACE, J. M. 2014 Space–time correlations in turbulent flow: a review. *Theor. Appl. Mech. Lett.* **4** (2), 022003.

WILLERT, C. E. 2015 High-speed particle image velocimetry for the efficient measurement of turbulence statistics. *Exp. Fluids* **56**, 17.

WILLERT, C. E., CUVIER, C., FOUCAUT, J. M., KLINNER, J., STANISLAS, M., LAVAL, J. P., SRINATH, S., SORIA, J., AMILI, O., ATKINSON, C. *et al.* 2018 Experimental evidence of near-wall reverse flow events in a zero pressure gradient turbulent boundary layer. *Exp. Therm. Fluid Sci.* **91**, 320–328.

https://doi.org/10.1017/jfm.2019.408 Published online by Cambridge University Press